AFRL-AFOSR-UK-TR-2013-0027

Dynamics of supercritical-pressure coaxial jets submitted to transverse acoustic modulations

Thomas Schmitt
Sebastien Ducruix
Sebastien Candel

Centrale Recherche SA
Ecole Centrale Paris
Grande Voie Des Vignes
Chatenay-Malabry, 92295 France

EOARD Grant 12-2047

Report Date: June 2013

Final Report from 08 March 2012 to 07 March 2013

Air Force Research Laboratory
Air Force Office of Scientific Research
European Office of Aerospace Research and Development
Unit 4515 Box 14, APO AE 09421

REPORT DOCUMENTATION PAGE

Form Approved OMB No. 0704-0188

1. REPORT DATE *(DD-MM-YYYY)*	2. REPORT TYPE	3. DATES COVERED *(From – To)*
24 June 2013	Final Report	08 March 2012 – 07 March 2013

4. TITLE AND SUBTITLE

Dynamics of supercritical-pressure coaxial jets submitted to transverse acoustic modulations

5a. CONTRACT NUMBER

FA8655-12-1-2047

5b. GRANT NUMBER

Grant 12-2047

5c. PROGRAM ELEMENT NUMBER

61102F

6. AUTHOR(S)

Thomas Schmitt
Sebastien Ducruix
Sebastien Candel

5d. PROJECT NUMBER

5d. TASK NUMBER

5e. WORK UNIT NUMBER

7. PERFORMING ORGANIZATION NAME(S) AND ADDRESS(ES)

Centrale Recherche SA
Ecole Centrale Paris
Grande Voie Des Vignes
Chatenay-Malabry, 92295 France

8. PERFORMING ORGANIZATION REPORT NUMBER

N/A

9. SPONSORING/MONITORING AGENCY NAME(S) AND ADDRESS(ES)

EOARD
Unit 4515
APO AE 09421-4515

10. SPONSOR/MONITOR'S ACRONYM(S)

AFRL/AFOSR/IOE (EOARD)

11. SPONSOR/MONITOR'S REPORT NUMBER(S)

AFRL-AFOSR-UK-TR-2013-0027

12. DISTRIBUTION/AVAILABILITY STATEMENT

Distribution A: Approved for public release; distribution is unlimited.

13. SUPPLEMENTARY NOTES

14. ABSTRACT

Large-Eddy Simulation of transcritical turbulent mixing is investigated in this report. This analysis is motivated by rocket propulsion applications where cryogenic oxygen is injected at low temperature, below the critical value, in a high pressure environment where the pressure is above critical. This situation is here envisaged by analyzing the behavior of a nitrogen jet delivered by a shear coaxial injector comprising an inner stream injected at temperatures close to the critical temperature and a coaxial flow at a higher temperature. Real gas Large Eddy Simulations are carried out for selected experiments previously performed at AFRL, Edwards Air Force Base (USA). Two geometrical configurations associated with two sets of mass flow rates have been studied at AFRL (LarThin and SarThick). They lead to different jet dynamics and subsequently different responses to acoustic modulation. Calculations retrieve what is observed experimentally both in the absence of an external modulation and under transverse acoustic field. It is shown in particular that in the LarThin case the acoustic forcing produces large scale transverse oscillations of the inner stream and promotes the formation of counter rotating vortices in the wake of the high density jet. These coherent structures stretch the inner jet, increasing the mass exchange surface between the two streams and the mixing efficiency. In the SarThick situation, a large scale back flow is established around the inner jet, which limit its downstream penetration promoting recirculation of cold fluid behind the thick lip. The acoustic modulation has a limited effect on the jet geometry in this case, probably because of the presence of this dynamic back flow region. The inner jet length is nevertheless reduced in a significant way.

15. SUBJECT TERMS

EOARD, supercritical injection, shear coaxial injectors, transverse acoustic modulation

16. SECURITY CLASSIFICATION OF:			17. LIMITATION OF ABSTRACT	18, NUMBER OF PAGES	19a. NAME OF RESPONSIBLE PERSON
a. REPORT	b. ABSTRACT	c. THIS PAGE			Kevin Bollino
UNCLAS	UNCLAS	UNCLAS	SAR	44	19b. TELEPHONE NUMBER *(Include area code)* +44 (0)1895 616163

Grand number FA8655-12-1-2047

Dynamics of supercritical-pressure coaxial jets submitted to transverse acoustic modulations.

Thomas Schmitt, Sébastien Ducruix and Sébastien Candel
EM2C, CNRS, Ecole Centrale Paris, 92295 Chatenay-Malabry, France

March 8th 2012 - March 7th 2013

Contents

List of Figures

Dynamics of supercritical-pressure coaxial jets submitted to transverse acoustic modulations. (Award FA8655-12-1-2047 - Final report)

Thomas Schmitt, Sébastien Ducruix and Sébastien Candel
EM2C, CNRS, Ecole Centrale Paris, 92295 Chatenay-Malabry, France

July 17, 2013

Abstract

Large-Eddy Simulation of transcritical turbulent mixing is investigated in this report. This analysis is motivated by rocket propulsion applications where cryogenic oxygen is injected at low temperature, below the critical value, in a high pressure environment where the pressure is above critical. This situation is here envisaged by analyzing the behavior of a nitrogen jet delivered by a shear coaxial injector comprising an inner stream injected at temperatures close to the critical temperature and a coaxial flow at a higher temperature. Real gas Large Eddy Simulations are carried out for selected experiments previously performed at AFRL, Edwards (USA). Two geometrical configurations associated with two sets of mass flow rates have been studied at AFRL (LarThin and SarThick). They lead to different jet dynamics and subsequently different responses to acoustic modulation. Calculations retrieve what is observed experimentally both in the absence of an external modulation and under transverse acoustic field. It is shown in particular that in the LarThin case the acoustic forcing produces large scale transverse oscillations of the inner stream and promotes the formation of counter rotating vortices in the wake of the high density jet. These coherent structures stretch the inner jet, increasing the mass exchange surface between the two streams and the mixing efficiency. In the SarThick situation, a large scale back flow is established around the inner jet, which limit its downstream penetration promoting recirculation of cold fluid behind the thick lip. The acoustic modulation has a limited effect on the jet geometry in this case, probably because of the presence of this dynamic back flow region. The inner jet length is nevertheless reduced in a significant way.

Keywords *: Supercritical injection, shear coaxial injectors, transverse acoustic modulation.*

1 Introduction

Modern liquid rocket engines, which use cryogenic propellants, commonly operate under transcritical conditions, a situation where the chamber pressure is above the critical point

and the injection temperature is below the critical value for at least one of the propellants. During the design phase of these engines, combustion instabilities (CI) may occur, which can stall or severely delay their development. CIs result from a complex coupling between acoustic modes of the chamber and the flow, mixing and heat release processes. The latter is usually structured by the inner and outer streams originating from a shear coaxial element (most common injector design for cryogenic engines), interacting with each other and with their surroundings. The dynamics and mixing of coaxial transcritical jets submitted to acoustic modulations is then of interest for the study of combustion instabilities. Moreover, studying the transient and unsteady phenomena occurring in such configurations is of fundamental importance for the understanding and prediction of cryogenic flow dynamics. This is here investigated by analyzing the behavior of a nitrogen shear coaxial jet comprising an inner stream injected at temperatures close to the critical temperature and a coaxial flow at a higher temperature. Experiments are carried out both in the absence of external modulation and by imposing a large amplitude transverse acoustic field. Real gas Large Eddy Simulations (LES) are performed for selected experiments. The combination of experiments and calculations is used to evaluate effects of the operating parameters on the coaxial jet response.

The interaction of transverse acoustic waves with transcritical flows and its influence on mixing efficiency has been considered in previous studies. The impact of acoustics on a non-reacting shear coaxial jet has been investigated experimentally by Leyva, Rodriguez et al. [15, 14, 4]. They found that the injector geometry has an effect on the sensitivity of the coaxial flows to acoustic modulation. This study has been continued recently, through a grant from EOARD, by considering the combination of experiments and simulations, in a collaboration between AFRL and EM2C [16]. This collaboration was quite productive in terms of shedding light on key experimental observations made at AFLR by using state of the art LES tools available at EM2C (see [17, 18] for an example of applications). Simulations were carried out with the AVBP-RG software jointly developed by Cerfacs and EM2C. By analyzing the spectral content of the LES flow field results, it was found that in this particular configuration the transcritical inner jet was relatively insensitive to the acoustic modulation, while the gaseous annular jet was strongly perturbed and generated large scale vortices. It was suggested that the relative insensitivity of the inner flow is linked to the fact that the frequency was above the range of preferred frequencies of the central jet. Key natural hydrodynamic instabilities were also determined with LES, which is of paramount importance to calculate which frequencies can interact with the combustion process.

The general goal is to continue these investigations on the mixing of coaxial transcritical jets submitted to acoustic modulations. In the previous collaborative study between AFRL and EM2C, a single injector geometry, with a thick inner jet lip separating the 2 streams, was considered. One particular objective of the present research is to assess the influence of geometrical parameters on the jet dynamics and sensitivity to acoustic modulation by using experimental data from AFRL on an alternate geometry, a thin lip injector [15]. Key experimental cases will be simulated using LES. It has been experimentally observed at AFRL that the flow in this alternative geometry, when exposed to acoustics, shows more visible effects such as a large shortening of the inner jet "intact" length. LES can help identify the mechanisms which define this dynamical behavior.

Both experiments and numerical simulations are used in the present study. Experiments

are carried out at AFRL while numerical simulations are performed at the EM2C laboratory. Experiments provide high speed shadowgraphs of the flow and average temperature profiles. From these data, simulations can be validated and results of calculations can then be used to augment the experimental measurements and visualizations in order to study the flow dynamics and identify the subtending processes.

2 Balance equations and models

This section provides a synthesis of the main equations and submodels used in the present simulations.

2.1 Governing equations

A single species flow configuration is investigated in the present investigation. In this situation, the vector of conservative variables for a compressible flow is $\boldsymbol{w} = (\rho, \rho\boldsymbol{u}, \rho E)^T$, where ρ is the density, $\boldsymbol{u}$ the velocity vector and E the total energy (E is the sum of internal energy e_s and kinetic energy $e_k = 1/2 \sum u_i^2$). The large-eddy simulations are carried out by integrating the mass weighted spatially filtered Navier-Stokes equations. In the following balance equations (for a given variable ϕ, $\overline{\phi}$ designates the spatially filtered variable, while $\tilde{\phi}$ is the mass-weighted (Favre) spatially filtered variable) :

$$\frac{\partial \overline{\rho}}{\partial t} + \frac{\partial \overline{\rho}\tilde{u_j}}{\partial x_j} = 0 \tag{1}$$

$$\frac{\partial \overline{\rho}\tilde{u_i}}{\partial t} + \frac{\partial \overline{\rho}\tilde{u_j}\tilde{u_i}}{\partial x_j} = -\frac{\partial \overline{p}}{\partial x_i} + \frac{\partial \overline{\tau_{ij}}}{\partial x_j} - \frac{\partial \tau_{ij}^t}{\partial x_j} \tag{2}$$

$$\frac{\partial \overline{\rho}\tilde{E}}{\partial t} + \frac{\partial \overline{\rho}\tilde{E}\tilde{u_j}}{\partial x_j} + \frac{\partial \overline{p}\tilde{u_j}}{\partial x_j} = -\frac{\partial \overline{q_j}}{\partial x_j} - \frac{\partial q_j^t}{\partial x_j} + \frac{\partial \tilde{u_i}\overline{\tau_{ij}}}{\partial x_j} \tag{3}$$

In Eqs. 1-3, p is the pressure, $\boldsymbol{x}$ the spatial coordinates vector and t is the time. The laminar viscous stress tensor $\boldsymbol{\tau}$ and heat flux vector $\boldsymbol{q}$ are expressed as linear functions of the strain rates and temperature gradient respectively. Laminar viscosity and heat conductivity coefficients are determined with the Chung *et al.* method [2]. For the single species case investigated in the present article, no additional diffusion terms are needed since the Soret and Dufour effects naturally vanish. The sub grid scale tensor τ_{ij}^t rely on the WALE model [7] and the subgrid scale heat flux is modeled using a standard gradient transport assumption :

$$\overline{q_i}^t = -\lambda_t \frac{\partial \widetilde{T}}{\partial x_i} \tag{4}$$

The subgrid scale conductivity is cast in the form $\lambda_t = c_p\mu_t/\mathrm{Pr}_t$ where $\mu_t = \rho\nu_t$ and Pr_t respectively designate the subgrid dynamic viscosity and turbulent Prandtl number. As in low pressure simulations a constant value $\mathrm{Pr}_t = 0.7$ is used in the present calculations.

2.2 Real gas thermodynamics and equation of state

Real gas thermodynamics for high pressure flow calculations is envisaged in many recent studies where accurate descriptions of the fluid state are derived from various types of equations [1, 21]. The present simulations rely on the Peng-Robinson equation of state (EOS) [10] (Eq. 5) which is used in the analysis to model the departure from an ideal-gas behavior. The fluid state is expressed in the form :

$$p = \frac{\rho r T}{1-\rho b} - \frac{\rho^2 a(T)}{1+2\rho b-\rho^2 b^2} \tag{5}$$

where T is the temperature, $r = R/W$ with R the perfect-gas constant and W the molar mass. The Peng-Robinson coefficients $a(T)$ and b for a single-species fluid are [12]:

$$a = 0.457236\frac{(rT_c)^2}{p_c}\left(1+c(1-\sqrt{T_R})\right)^2 \tag{6}$$

$$b = 0.077796\frac{rT_c}{p_c} \tag{7}$$

with

$$c = 0.37464 + 1.54226\omega - 0.26992\omega^2 \tag{8}$$

where $T_c = 126.2$ K and $p_c = 3.396$ MPa are the critical temperature and pressure of nitrogen, $\omega = 0.0372$ represents its acentric factor and $T_R = T/T_c$ is the reduced temperature. This equation offers a good trade-off between computational cost and precision. The pressure dependence of thermodynamic functions and coefficients is subsequently derived from the EOS [5, 8, 21].

3 Computational setup

3.1 Numerical aspects

The mass weighted spatially filtered compressible Navier-Stokes equations in combination with the subgrid scale models described previously are integrated in the AVBP flow solver [19, 6]. The present integration method relies on a Taylor-Galerkin weighted residual central distribution scheme, called TTGC. This scheme is third-order in space and third-order in time [3].

The real gas equation of state, thermodynamics and transport coefficients have been implemented in AVBP. The convective fluxes Jacobian matrices, used by the scheme, are expressed in terms of real gas thermodynamics to preserve the overall consistency of the code. A fully consistent treatment of associated boundary conditions is based on the characteristic wave decomposition method NSCBC [11, 6] and includes specific expressions provided for real gas thermodynamics in [9]. The treatment of steep gradients relies on artificial viscosity and is activated when unresolved gradients are detected by a density-based sensor. More details about the sensor and the operators used to trigger artificial viscosity addition can be found in [16].

3.2 Computational domain

The mixing chamber used in the simulation is shown in Fig. 1a. Its dimensions corresponds to the experimental ones, with a chamber length of 59.4 mm, and a rectangular section of 12.7 × 76 mm. In the experiment, in order to maintain the pressure in the chamber, the chamber is placed inside a larger pressurization system. The two chambers are connected through an upstream perforated plate and through the outlet pipe. The velocity through the perforated plate is thus not imposed, but results from entrainment by the coaxial jet. This geometry can be qualitatively accounted for in the simulation by placing an upstream large volume as shown in Fig. 1b.
In order to assess the influence of the perforated plate holes, preliminary simulations were carried out with and without the upstream reservoir. When the the upstream reservoir is not used, an inlet velocity is imposed at the perforated walls. Two values for the inlet velocity are compared: 1 m s^{-1} and 0.1 m s^{-1} to test the sensitivity to this parameter. Results are plotted in Fig. 2 for a set of radial profiles. This shows that the profiles are close to each other. Thus an injection velocity can be imposed at the hole exhaust section, which simplifies the computational domain and lowered the mesh requirement. A value of 1 m s^{-1} is chosen in the calculations.

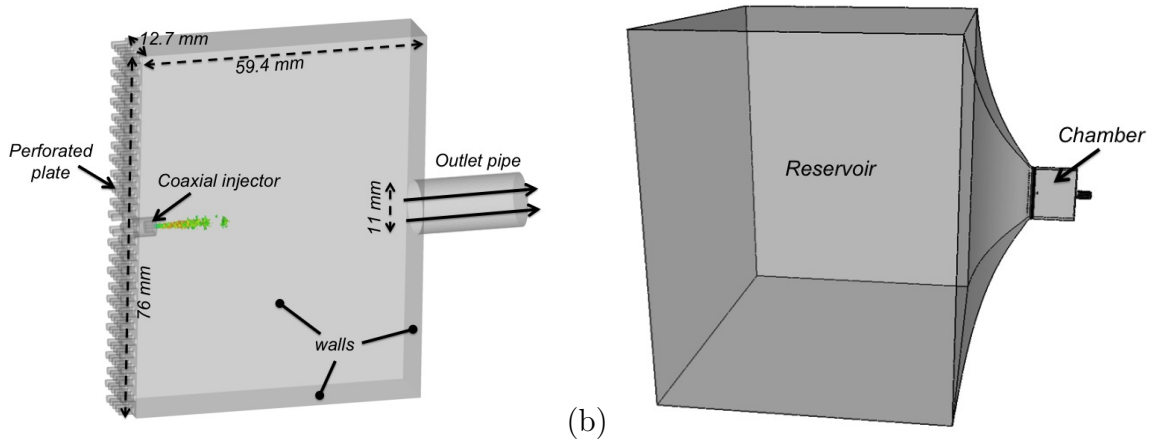

Figure 1: *Computational domain* (a) Mixing chamber (b) Domain with the upstream reservoir connected to the perforated plate. Preliminary simulations show that the upstream reservoir can be neglected for the simulations, and a low velocity injection can be imposed at the perforated plane inlets instead.

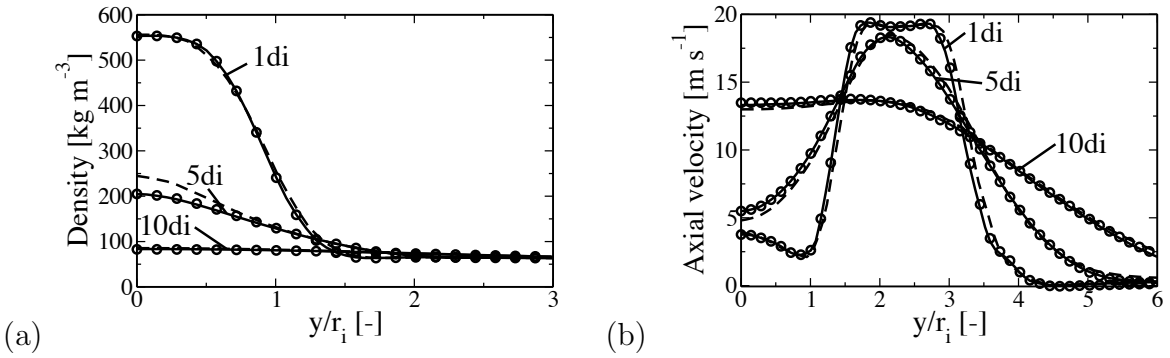

Figure 2: Influence of perforated walls boundary conditions. Imposed inlet velocity: ∘ 0.1 m/s — 1 m/s ; with an upstream reservoir — —.

3.3 Injector geometries and mesh definitions

Two injector geometries are considered in this study. They differ by the thickness of the inner lip and the surface area ratio between the outer and inner injection plane. They are referred to as LarThin (Large aspect ratio, Thin lip) and SarThick (Small aspect ratio, Thick lip). Their characteristics are given in Tab. 1.

Case	δ_l [mm]	S_e/S_i	d_i [mm]	h_e [mm]
LarThin	0.095	10.6	0.7	0.775
SarThick	1.13	2.9	1.47	0.37

Table 1: Injector geometrical parameters. δ_l is the inner lip thickness, S_e the outer injector section surface, S_i the inner post section surface, d_i the inner injector diameter and h_e the outer injector thickness.

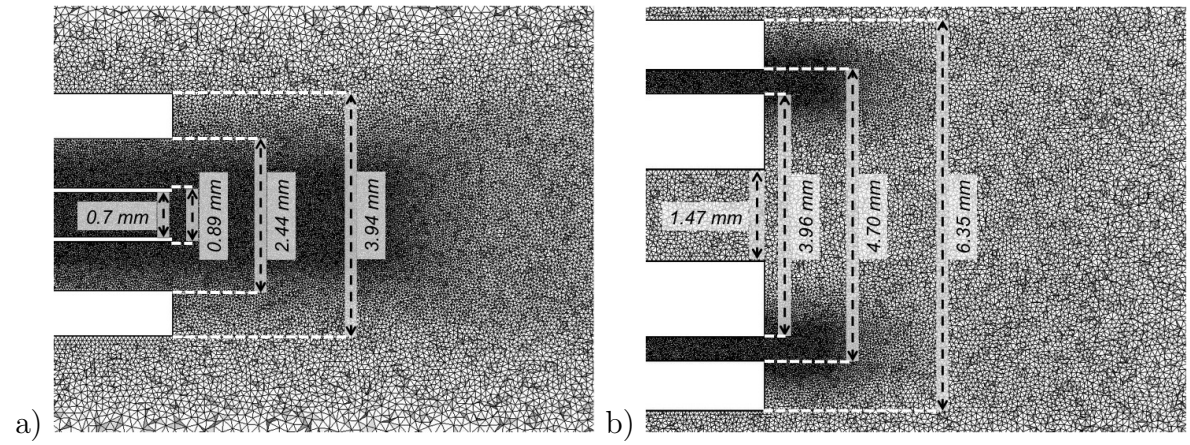

Figure 3: Longitudinal slice of the meshes (near injector region) (a) LarThin (b) SarThick. SeeTab. 2 for details

Longitudinal slices of the meshes for cases LarThin and SarThick are shown on Fig. 3

and 4. They are both fine near the injector with a smooth coarsening toward exit. For SarThick simulations, the mesh is refined in the annular injector in order to ensure a proper turbulence resolution. The grid characteristics are detailed in Tab. 2. Both meshes comprise approximately 20 million cells, with 30 cells along the inner and outer injector characteristic length for case LarThin, and 20 and 15 cells in the inner and outer injectors for case SarThick. A grid sensitivity study is proposed in Sec. 5.

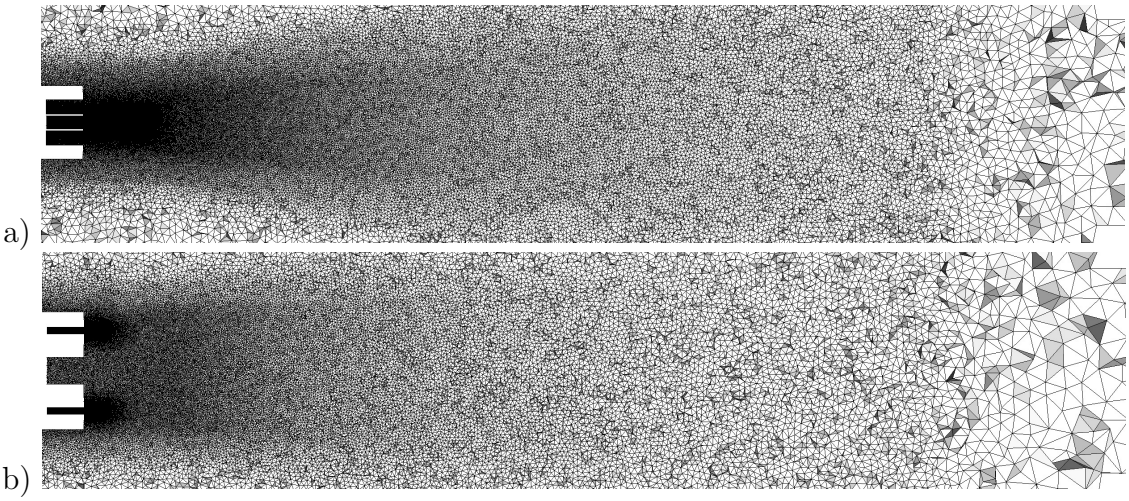

Figure 4: Longitudinal slice of the mesh (a) LarThin (b) SarThick (Tab. 2)

Case	Nb of cells	Δt [s]	CPU time for 1 τ_c [h]	Δx_{min} [mm]
LarThin	20 944 365	$1.9\ 10^{-8}$	10 200	0.025
SarThick	23 664 745	$1.9\ 10^{-8}$	38 750	0.0245

Table 2: Characteristics of the mesh used for the simulations. Δt is the time step, $\tau_c = 25 d_{inner}/u_{inner}$ the convective time.

3.4 Injection characteristics and boundary conditions

These simulations consider pure nitrogen injected in a chamber at a pressure of 3.56 MPa for both cases. The chamber temperature is 223 K for case LarThin and 205 K for case SarThick. Injection conditions for the simulated cases are given in Tab. 3 and 4. The two cases have comparable density ratio between the outer and inner injection channels (7.7 for LarThin and 9.0 for SarThick). There is a slight departure between the two cases considering the velocity ratio (6.5 for LarThin and 9.0 for SarThick), which leads to a higher momentum flux ratio for case SarThick than for LarThin (9.2 vs 5.0).
All the solid boundaries in the simulation are treated as no slip adiabatic walls. Pressure is imposed at the outlet using a partially non-reflecting characteristic boundary condition. Flat profiles are injected at the perforated plate. Fully turbulent profiles are assumed at injector inlets with anisotropic turbulent fluctuations superimposed to the mean flow profile at the injector inlet (Fig. 5) [20].

Case	T_i [K]	u_i [m s^{-1}]	ρ_i [kg m^{-3}]	T_e [K]	u_e [m s^{-1}]	ρ_e [kg m^{-3}]
LarThin	122	2.5	531	203	16.2	63
SarThick	120	2.1	556	203	18.9	63

Table 3: Injection characteristics of the simulated cases. ρ_i, ρ_e, u_i, u_e, T_i and T_e are the inner and outer jet densities, velocities and temperature.

Case	$J = (\rho_e u_e^2)/(\rho_i u_i^2)$	$M = (\rho_e u_e)/(\rho_i u_i)$	$S = \rho_i/\rho_e$	$U = u_e/u_i$
LarThin	5.0	0.77	7.7	6.5
SarThick	9.2	0.72	9.0	9.0

Table 4: Injection characteristics of the simulated cases. J is the momentum flux ratio between the outer and the inner jets, M the mass flux ratio, S the density ratio and U is the velocity ratio. ρ_i, ρ_e, u_i and u_e are the inner and outer jet densities and velocities.

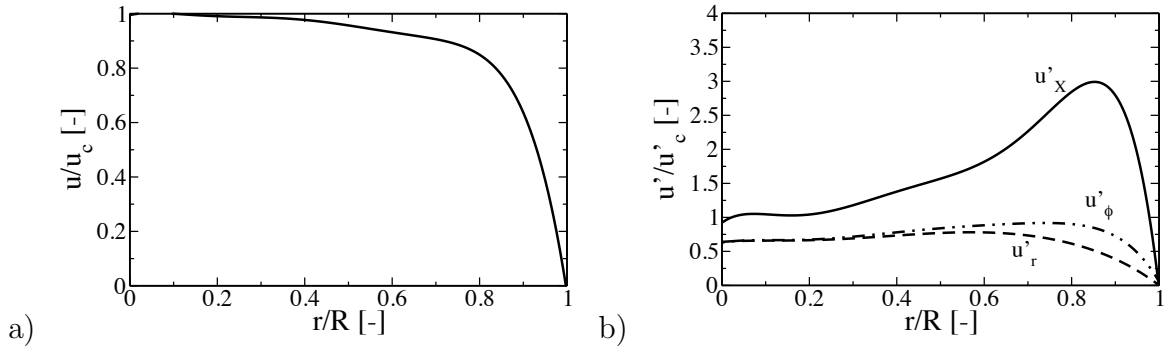

Figure 5: Radial velocity profiles at injection for both inlet. (a) Axial mean velocity u, normalized by its centerline value u_c, (b) axial , azimuthal and radial rms velocities (u'_x, u'_ϕ and u'_r, respectively).

4 Grid sensitivity study

To estimate the grid sensitivity calculations are carried out for the two geometries on three different meshes referred as "coarse", "intermediate" and "fine". Their characteristics are detailed in Tab. 5. They all share the same cell distribution, shown in Fig. 4 and only differ by the smallest characteristic cell size Δx_{min} present in the grid. Comparisons between results obtained with the three meshes indicates that the intermediate mesh is adequate. This mesh is used in the final simulations in this document. This study requires large CPU resources and it is important to sure make sure that the calculations are accurate but with a minimal expenditure of CPU time.

Case	Nb of cells	Δt [s]	CPU for 1 τ_c [h]	Δx_{min} [mm]
LarThin coarse	6 237 282	$2.9\ 10^{-8}$	2 000	0.0375
LarThin intermediate	20 944 365	$1.9\ 10^{-8}$	10 200	0.025
LarThin fine	77 301 292	$1.05\ 10^{-8}$	68 000	0.017
SarThick coarse	8 180 162	$2.8\ 10^{-8}$	11 600	0.035
SarThick intermediate	23 664 745	$1.9\ 10^{-8}$	38 750	0.0245
SarThick fine	64 763 744	$1.4\ 10^{-8}$	151 000	0.0175

Table 5: Grid characteristics of the simulated cases. Δt is the time step, $\tau_c = 25 d_i/u_i$ the convective time.

4.1 Case LarThin

Longitudinal profiles of mean and rms densities obtained with the three meshes are shown in Fig. 6ab for case LarThin. The fine and intermediate grids feature results which are essentially identical. The same observations are made for radial profiles of density (Fig. 6c), with additional resolved density fluctuations in the near injector region as the grid is refined, as expected (Fig. 6d). The intermediate grid is thus well suited to the simulation of case LarThin and is used in this study.

4.2 Case SarThick

The same study as for case LarThin is carried out for the case SarThick. Longitudinal profiles of mean and rms densities are shown in Fig. 7ab. Again, the intermediate and fine grid profiles are close, but a small departure is noticeable at $x = 2d_i$, after the sudden density decrease. This region is characterized by a strong back flow and high turbulence level. This departure at $x = 2d_i$ is also present in the radial profiles shown in Fig. 7cd, while the other radial profiles are similar for intermediate and fine grids. Since the physical phenomena are captured by both grids (sudden decrease of density due to the presence of a back flow) and differences are limited and considering the large amount of CPU time required by the fine grid, it is reasonable to use the intermediate mesh used for all further simulations.

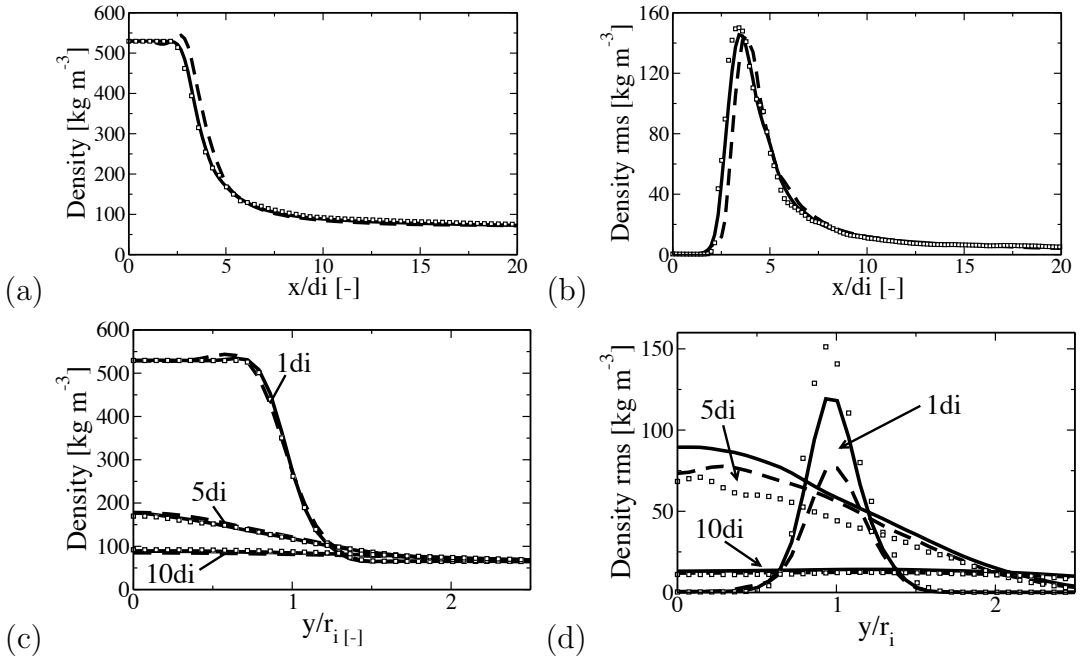

Figure 6: *Case LarThin - grid convergence study.* Longitudinal profiles of (a) mean, (b) rms densities and radial profiles of (c) mean and (d) rms densities. — — coarse —— intermediate □ fine

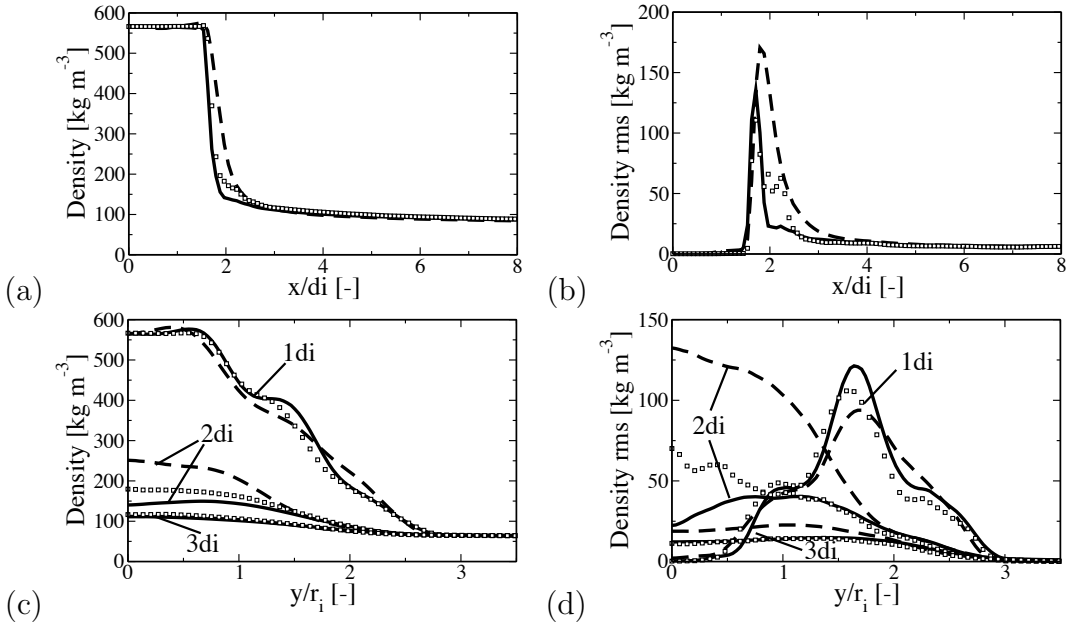

Figure 7: *Case SarThick - grid convergence study.* Longitudinal profiles of (a) mean, (b) rms densities and radial profiles of (c) mean and (d) rms densities.— — coarse —— intermediate □ fine

5 Results without modulation

This section is concerned with the modulation free cases. Results from simulations are first compared with the available experimental data in Sec. 5.1. and discussed in Sec. 5.2 and 5.3.

5.1 Comparisons with experimental data

Simulations are first compared with shadowgraph images. In the dark core light is deviated by changes in the refraction index. This in turn delineates regions where the density takes large values. It is generally admitted that the dark region represents the position of the dense core and highlights its external boundary giving an insight into the main structures present in the flow. Because the shadowgraph images integrate deviations over the line of sight, it is natural to integrate density or density gradients obtained numerically over the line of sight and compare these integrated maps with experimental data. Whatever the method, the comparison will remain essentially qualitative.
Results for case LarThin are shown in Fig. 8. The simulation properly retrieves the jet spreading rate and is in good qualitative agreement in terms of jet penetration.

Case SarThick is shown in Fig. 9. Simulations retrieve a short "dark core", as observed experimentally. Moreover, the density-integrated visualization properly reproduces the jet pinching observed experimentally. This comparison shows that the main feature of the flow are well retrieved by the simulation. Since density-integrated results are in good agreement with experimental images for both cases Larthin and SarThick, they will be used for all other experimental comparisons.
Finally, radial profiles of average temperature at one inner injector diameter are compared with experimental measurements in Fig. 10. Simulation results properly follow experimental curves for case LarThin: the plateaux are well retrieved and slopes are in good agreement. Case SarThick shows reasonable agreement with experiment, but there are some small departures in the outer region. They cannot be attributed to a limited grid resolution, as shown by the grid convergence study. At this point in time, the reason for this small departure is not found, but may be due to the adiabatic wall condition used at the lip. However, the study of heat transfer at the lip is out of the scope of the present work.

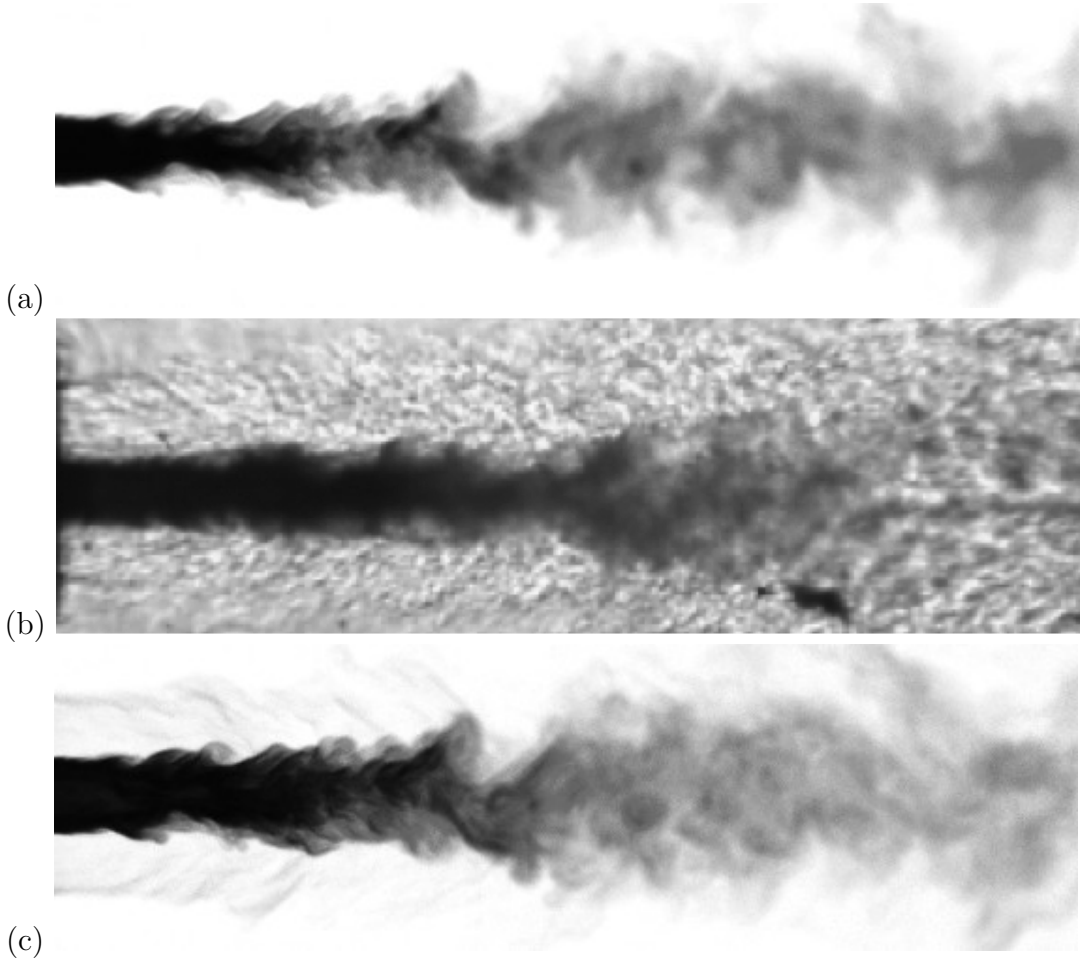

Figure 8: *Case LarThin* Qualitative comparison between backlighting images from (b) experiment and (a) (c) simulation. Density is integrated along the line of sight in (a), while density gradient is integrated in (c).

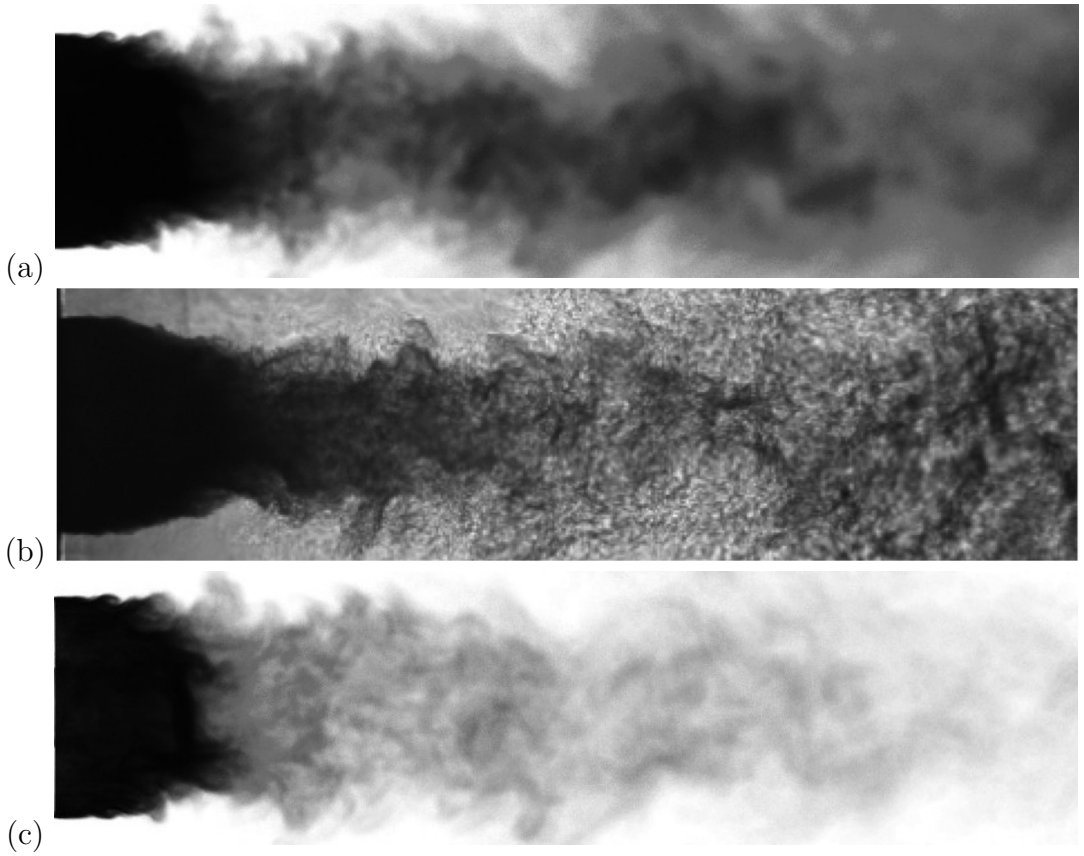

Figure 9: *Case SarThick* Qualitative comparison between backlighting images from (b) experiment and (a) (c) simulation. Density is integrated along the line of sight in (a), while density gradient is integrated in (c).

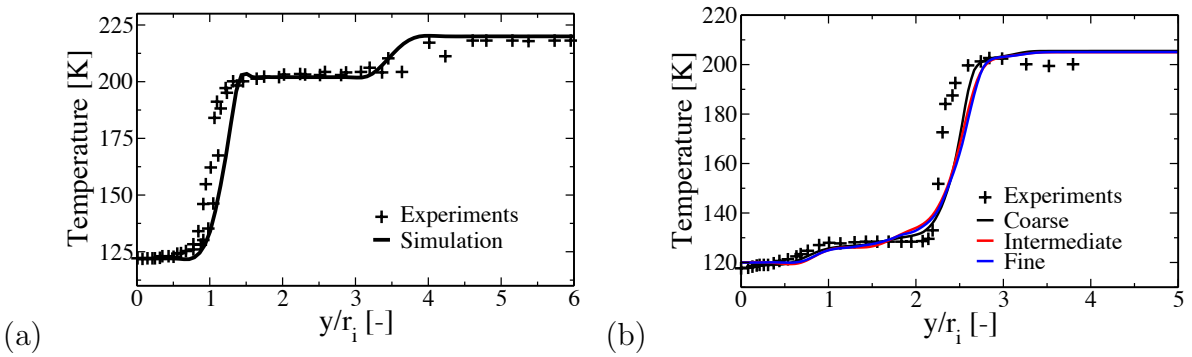

Figure 10: Radial profile of temperature at one injector diameter (a) Case LarThin (b) Case SarThick.

5.2 Instantaneous flow visualizations

Longitudinal slices of axial velocity are shown in Fig. 11 for cases LarThin and SarThick. The outer jet is injected at a higher velocity than the inner jet, producing a shear between the two streams that promotes the inner jet destabilization. The inner high density jet is then rapidly mixed with the surrounding gas. In both cases, the flow is fully turbulent. However, the flow structure differs between the two cases. While for case LarThin, the outer jet qualitatively follows the inner jet centerline axis direction, it is quickly bent toward the inner jet injection plane for case SarThick. In this latter case, a recirculation region is present behind the high density jet, which explains the sudden density drop observed in Fig. 7. A large scale recirculation is established behind the inner thick lips, where mass entrained from the inner jet mixes with hotter gas.

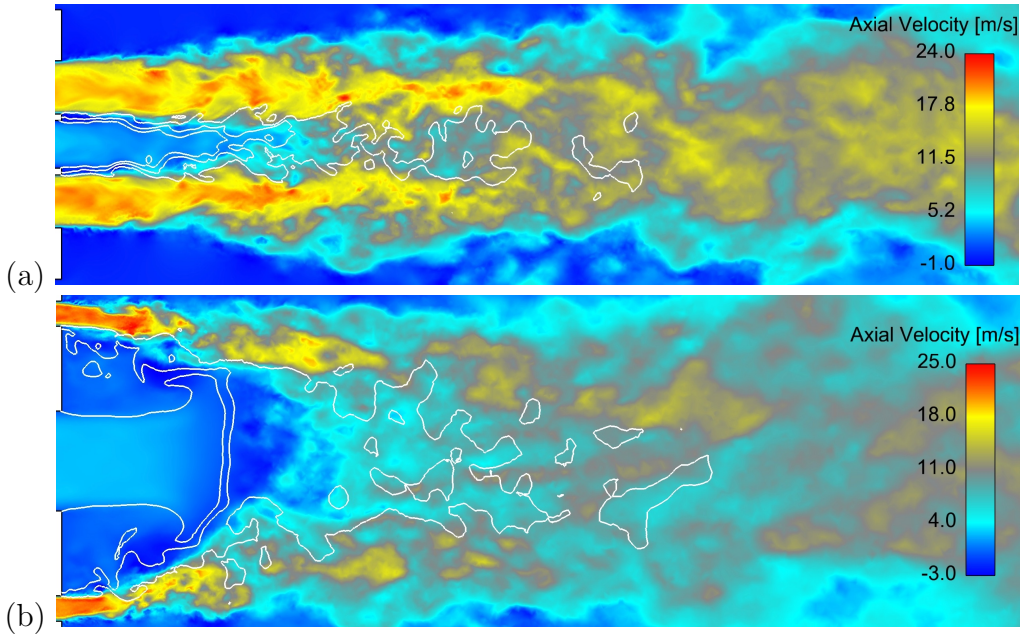

Figure 11: Longitudinal slice of axial velocity with iso-lines of density (100, 300 and 500 kg m^{-3}) (a) *Case LarThin* (b) *Case SarThick*.

Instantaneous iso-surfaces of density are shown in Fig. 12 and 13 for cases LarThin and SarThick. Turbulence strongly wrinkles the jet surface. Fig. 11b and 12b qualitatively show less wrinkling than the one observed on Fig. 11a and 12a, suggesting that the lower density regions are more affected than the higher density part of the flow. Fig. 12b and 13b highlight the major differences in terms of jet geometry between the two cases. The flow is confined by the back flow region surrounding the inner jet for case SarThick and cold nitrogen recirculates behind the thick lip (Fig. 13b).

5.3 Average fields

Longitudinal slices of mean and rms densities, mean and rms axial velocities are shown in Figs. 14 and 16 for case LarThin and in Figs. 15 and 17 for case SarThick. For both cases, a recirculation is generated behind the inner and outer lips. This region completely

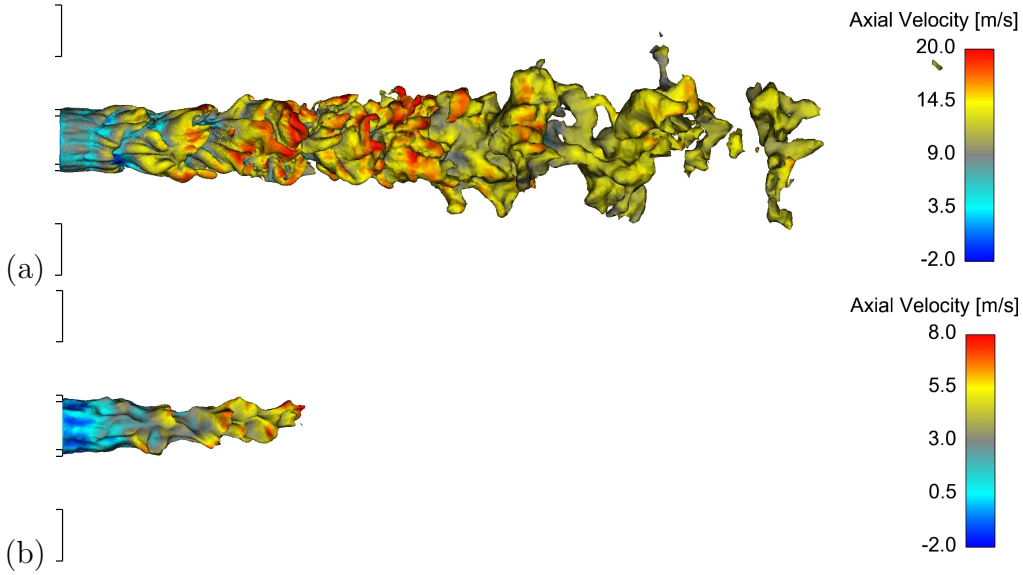

Figure 12: *Case LarThin*. Density iso-surfaces colored by axial velocity (a) 86 kg m^{-3} (b) 300 kg m^{-3}.

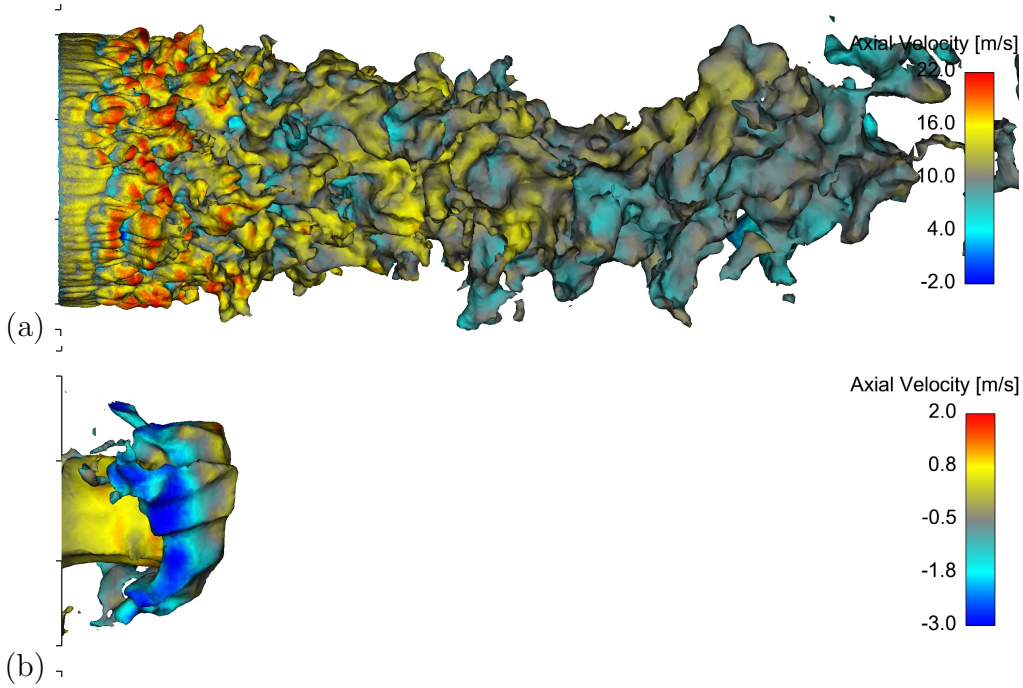

Figure 13: *Case SarThick*. Density iso-surfaces colored by axial velocity (a) 86 kg m^{-3} (b) 400 kg m^{-3}.

surrounds the inner jet in the SarThick case. As a consequence, cold nitrogen is entrained from the inner jet and deviated towards the recirculation region behind the lips in the SarThick case, while the inner stream propagates downstream in LarThin case. Plots of axial velocity are shown in Fig. 18, where the recalcirculation regions are clearly apparent for case SarThick in contrast with the case LarThin.

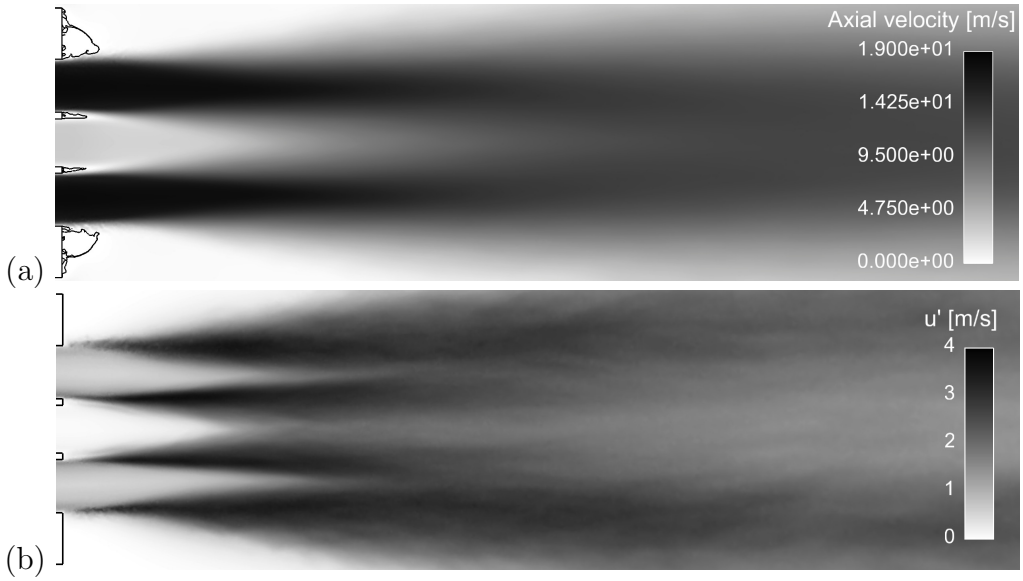

Figure 14: *Case LarThin.* Longitudinal slices of (a) mean axial velocity and (b) rms axial velocity.

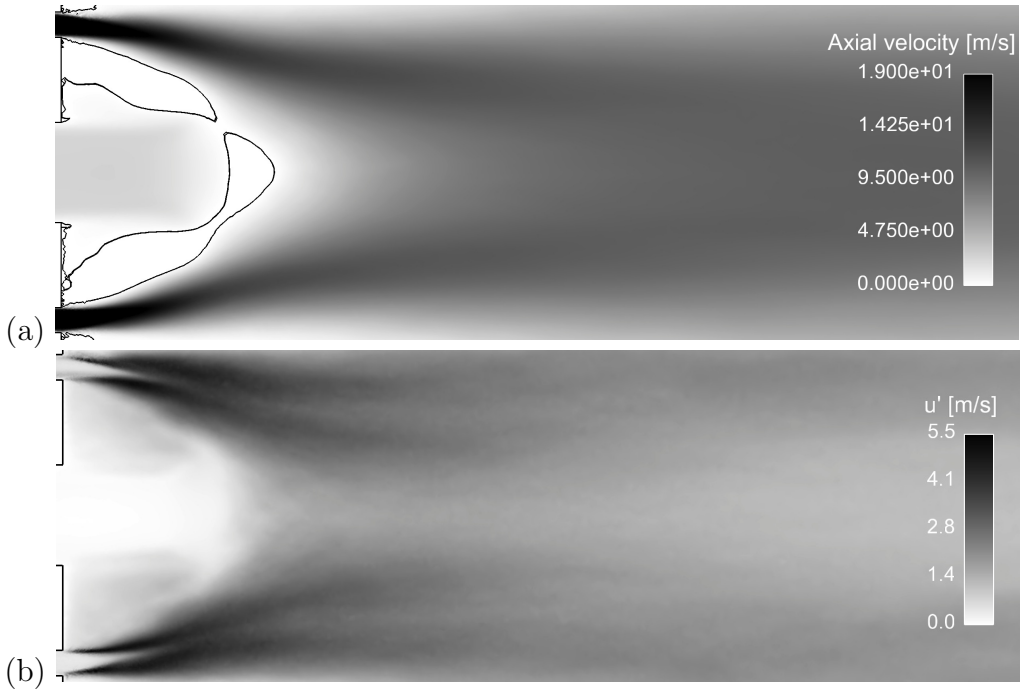

Figure 15: *Case SarThick*. Longitudinal slices of (a) mean axial velocity and (b) rms axial velocity.

Figure 16: *Case LarThin*. Longitudinal slices of (a) mean density and (b) rms density.

Figure 17: *Case SarThick*. Longitudinal slices of (a) mean density and (b) rms density.

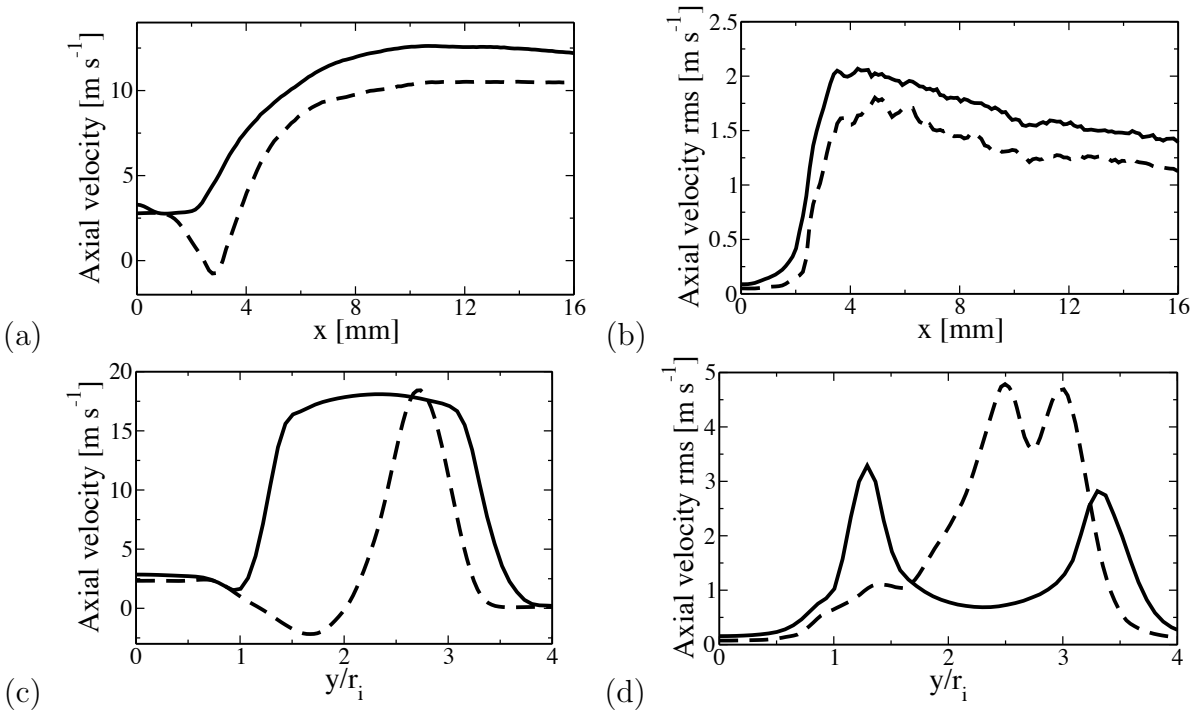

Figure 18: Longitudinal profiles of (a) mean axial velocity and (b) rms axial velocity, Radial profiles at 1 inner injector diameter, (c) mean axial velocity and (d) rms axial velocity. — Case LarThin – – case SarThick.

6 Modulated cases

The modulation free cases described previously were essentially meant to further validate the numerical simulation methodology. It is now possible to examine modulated cases. This section begins with a description of the modulation procedure. Results of simulations are then compared with experimental data.

6.1 Modulation procedure and simulated cases

An acoustic modulation is obtained by imposing harmonic modulations of the normal velocity at the outer boundaries using a method devised by Rey *et al.* [13]. The modulation has the form :

$$v_1 = A\sin(2\pi ft) \qquad v_2 = A\sin(2\pi ft + \pi) \tag{9}$$

where v_1 and v_2 are the normal velocities at the lateral boundaries, A the modulation amplitude and f is the modulation frequency set equal to 3.41 kHz. These boundaries are essentially acoustically non-reflecting (with a cut-off frequency of 100 Hz) in order to avoid the emergence of transverse eigenmodes. All other boundaries are treated as in the previous cases (in the absence of modulation). The normal velocities at the boundaries are in phase opposition, the jet is then placed in a velocity anti-node (maximum transverse velocity oscillation) and pressure node (no acoustic pressure oscillations along the jet centerline).
Modulated cases are gathered in Tab. 6. Two modulation amplitudes are considered: 1 and 2 m s^{-1}. These amplitudes are higher than those used in the experiment and are chosen to highlight the driving mechanisms.

Case	Geometry and injection conditions	f [Hz]	u'$_{ac}$ [m s^{-1}]
LarThin^2	LarThin	3 410	2
LarThin^1	LarThin	3 410	1
SarThick^2	SarThick	3 410	2
SarThick^1	SarThick	3 410	1

Table 6: Injection characteristics of the modulated cases. $u'_{ac} = 2A$ is the acoustic velocity modulation amplitude along the jet centerline.

6.2 Comparisons with experimental data

Instantaneous results are compared with experimental data for case LarThin in Fig. 19 by integrating the density over the line of sight. One notices that the sinusoidal motion observed in the experiment is well retrieved by the simulations.
Comparisons for case SarThick are shown in Fig. 20. Again, the jet behavior is qualitatively recovered. Both experiment and simulation feature an abrupt termination and t the jet pinching observed previously without acoustic modulation is no longer present.

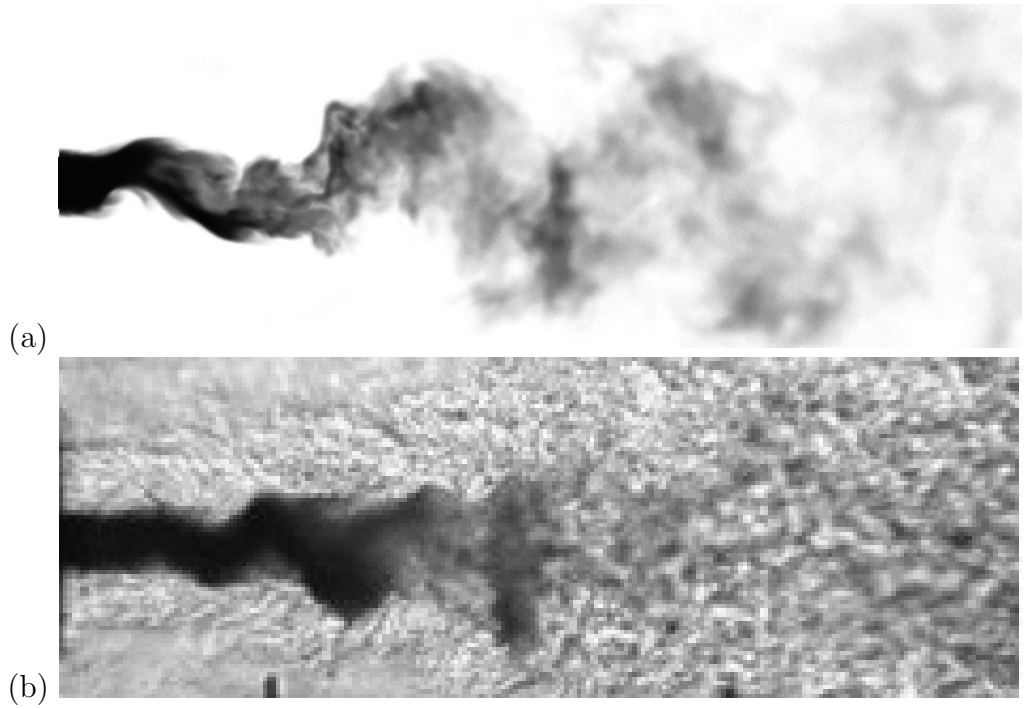

Figure 19: *Case LarThin*[1] Qualitative comparison between backlighting images from (b) experiment and simulation (a). Numerical results show density integrated over the line of sight.

6.3 Averaged fields

6.3.1 Case LarThin

Longitudinal slices showing the mean and rms densities are given in Fig. 21. The jet spreading rate is strongly increased compared to the unmodulated case (Fig. 16) and density fluctuations are now very high in the near vicinity of the injector exhaust. The axial velocity (Fig. 22) is quickly disturbed by the acoustic modulation, and strong velocity fluctuations are created near the injector exit due to the formation of large scale vortices which are alternatively released. Both in terms of density and axial velocity, the flow is more rapidly homogenized than in the unmodulated case, indicating that mixing is improved.

The acoustic modulation induces an important reduction of the jet penetration, which can be quantified from Fig. 23. The jet intact core length (distance from the injector of the section at which the density reaches 99 % of the injection density) is reduced to 0.30 of the unmodulated case for case LarThin[2]. Intact core length reduction falls to 0.4 times the unmodulated length for case LarThin[1]. The principal characteristic values are gathered in Tab. 7.

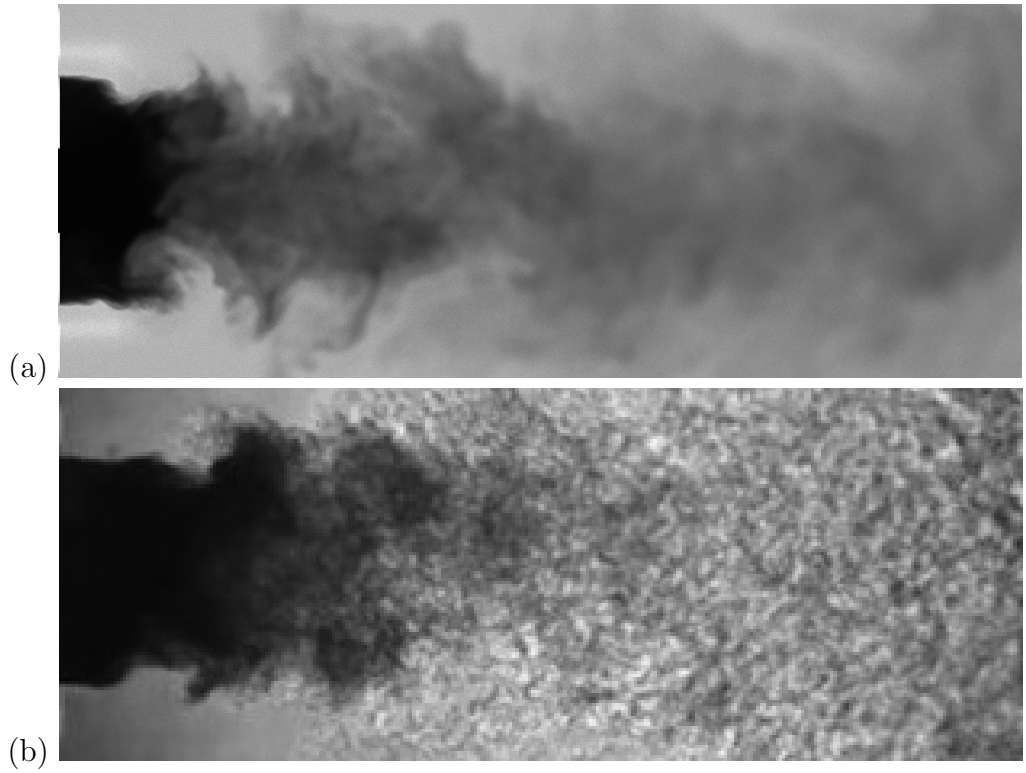

Figure 20: *Case SarThick*[1] Qualitative comparison between backlighting images from (b) experiment and simulation (a). Numerical results show density integrated over the line of sight.

Figure 21: *Case LarThin*[2]. Longitudinal slice of (a) mean density and (b) rms density.

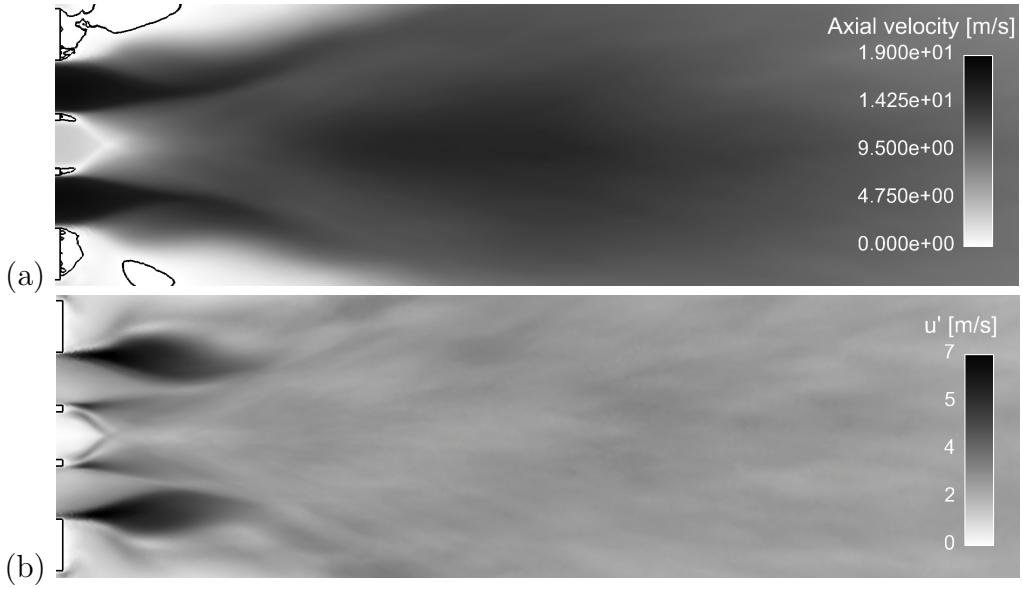

Figure 22: *Case LarThin*^{2}. Longitudinal slice of (a) mean axial velocity and (b) rms axial velocity.

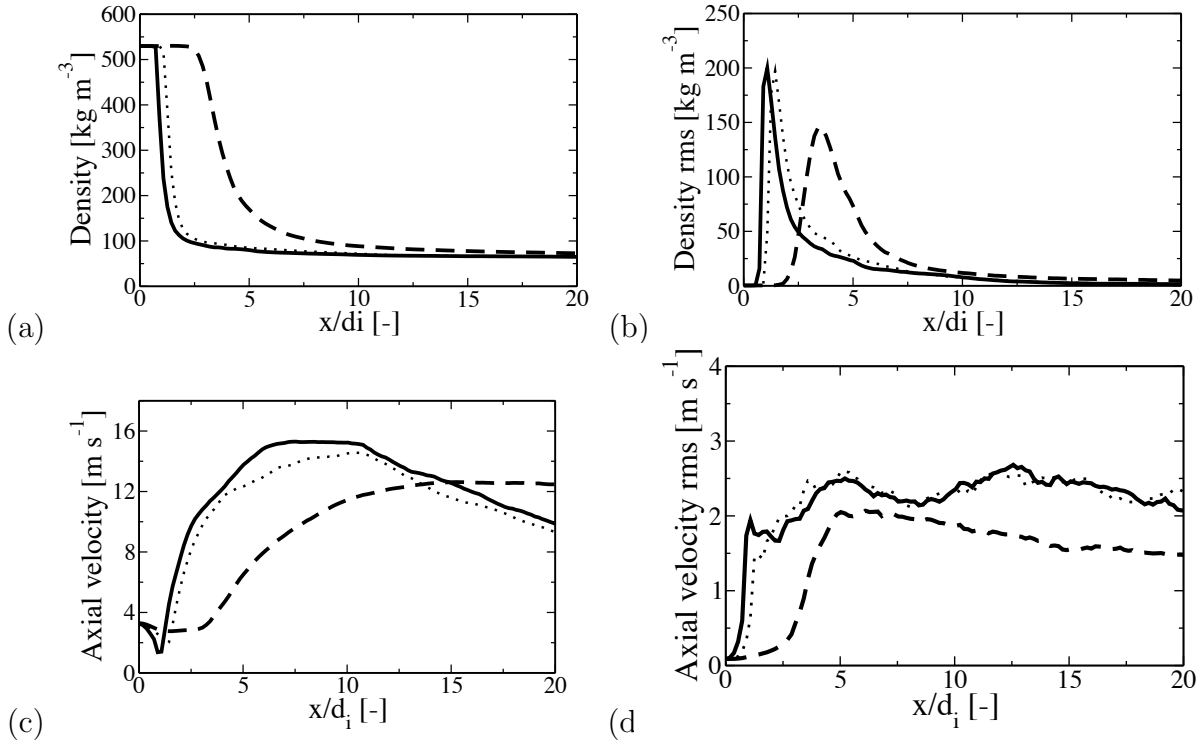

Figure 23: Longitudinal profiles of (a) mean density, (b) rms density, (c) mean axial velocity and (d) rms axial velocity. — Case LarThin^2 · · · Case LarThin^1 — — Case LarThin

Case	LarThin	LarThin^1	LarThin^2
L_ρ^{ic}	2.43 d_i	0.98 d_i	0.73 d_i
L_ρ^{ic} / $L_\rho^{ic,0}$	1	0.40	0.30

Table 7: Intact core length L_ρ^{ic} for cases LarThin, LarThin^2 and LarThin^1. $L_\rho^{ic,0}$ is the intact core length for the unmodulated case.

6.3.2 Case SarThick

Case SarThick less affected by the modulation than the case LarThin. The density field keeps the same geometry (Fig. 24) as that found in the modulation free case (Fig. 17), with a short high density core and the recirculation of cold nitrogen behind the lips. The size of the recirculation region that surrounds the inner jet is nevertheless augmented (Fig. 25).

Figure 24: *Case SarThick*^{2}. Longitudinal slice of (a) mean density and (b) rms density.

Due to the acoustic modulation, the intact core length of the inner jet is once again notably reduced compared with the unmodulated case (Fig. 26). The jet intact core length is reduced to 0.40 of the unmodulated case for case SarThick^2 and to 0.51 for case SarThick^1. Intact core lengths are gathered in Tab. 8.

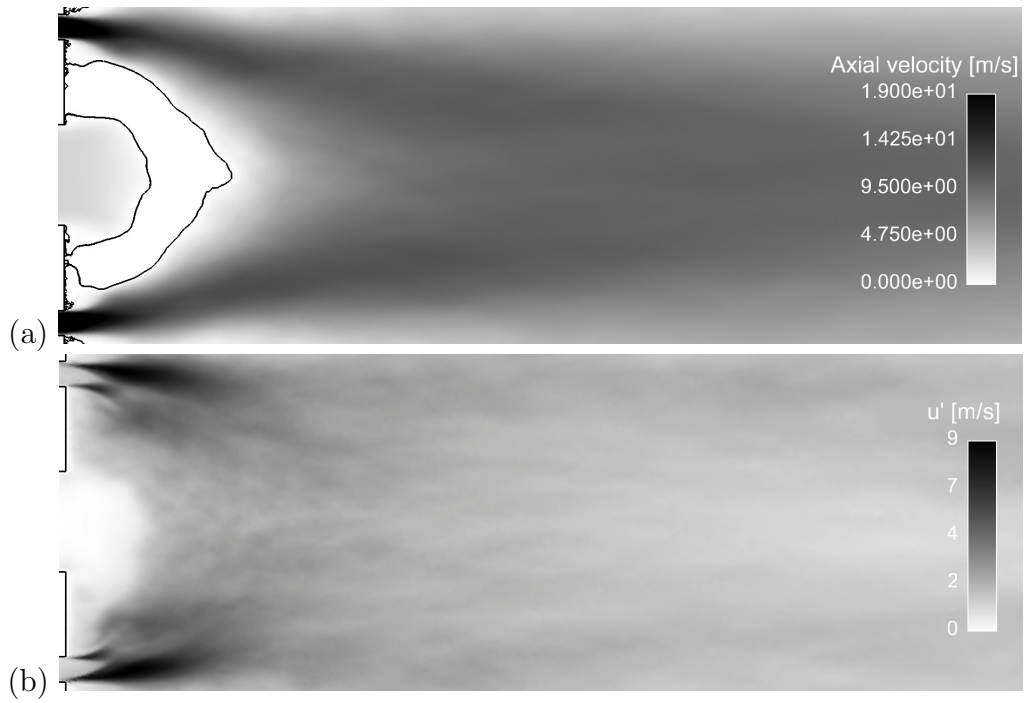

Figure 25: *Case SarThick*^{2}. Longitudinal slice of (a) mean axial velocity and (b) rms axial velocity.

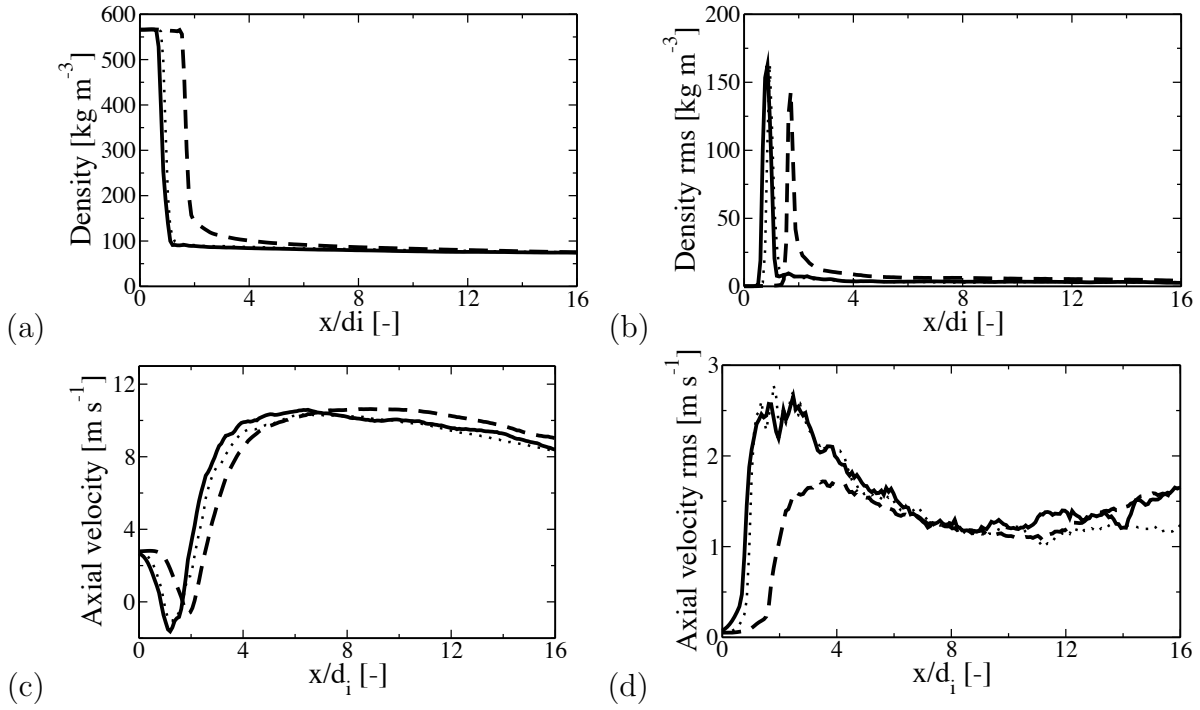

Figure 26: Longitudinal profiles of (a) mean density, (b) rms density, (c) mean axial velocity and (d) rms axial velocity. — Case SarThick^2 · · · Case SarThick^1 – – Case SarThick

Case	SarThick	SarThick^1	SarThick^2
L_ρ^{ic}	1.52 d_i	0.77 d_i	0.61 d_i
L_ρ^{ic} / $L_\rho^{ic,0}$	1	0.51	0.40

Table 8: Intact core length L_ρ^{ic} for cases SarThick, SarThick^2 and SarThick^1. $L_\rho^{ic,0}$ is the intact core length for the modulation free case.

6.4 Flow dynamics

6.4.1 Case LarThin

Instantaneous iso-surfaces of density (86 kg m^{-3}) over a half period are shown in Fig. 27. The transverse motion of the inner jet starts at the injector exit and is amplified further downstream. The jet quickly breaks down into several isolated small pockets that are eventually mixed with the surrounding hotter gas. Vortices are alternatively created at the injector exit (Fig. 28). They are quickly destroyed by turbulence further downstream. The high density jet is initially pinched by the modulation. The resulting thinned high density layer is wrinkled by turbulence and finally mixes with the outer jet.
In order to highlight periodic phenomena and remove wrinkling due to turbulence, phase averaged fields are computed over 20 periods of modulation. This limited number of periods is sufficient to get rid of most stochastic fluctuations.These fields are shown in Fig. 29. The acoustic modulation generates large scale counter rotating vortices that stretch the inner jet, creating the thin layer observed in Fig. 28. This phenomenon can be properly visualized in Fig. 33. The acoustic flow circumvents the high density stream and recirculates behind the high density inner jet. The lower density stream is notably influenced by the acoustic forcing and is peeled away from the inner jet forming the large scale vortices than can be seen in Fig. 29.
This dynamical behavior induces the complex motion observed in Fig. 27. Coupling Large Eddy Simulations and phase locked averaging techniques makes it possible to decompose this motion into the elementary processes that are observed in Fig. 29.

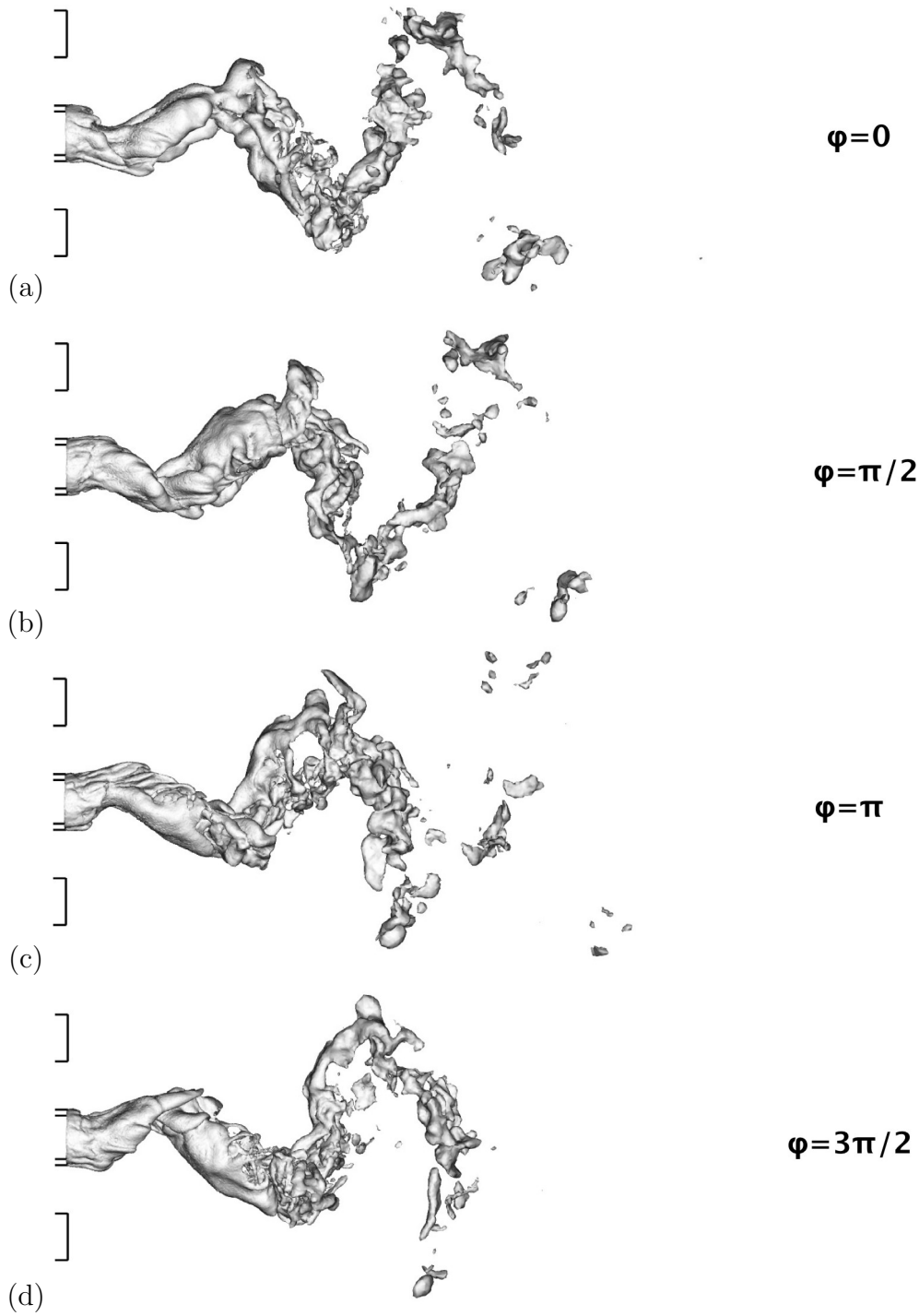

Figure 27: *Case LarThin*[2]. Density iso-surface (86 kg m^{-3}) during 4 phases ϕ of one period (a) $\phi = 0$ (b) $\phi = \pi/2$ (c) $\phi = \pi$ (d) $\phi = 3\pi/2$.

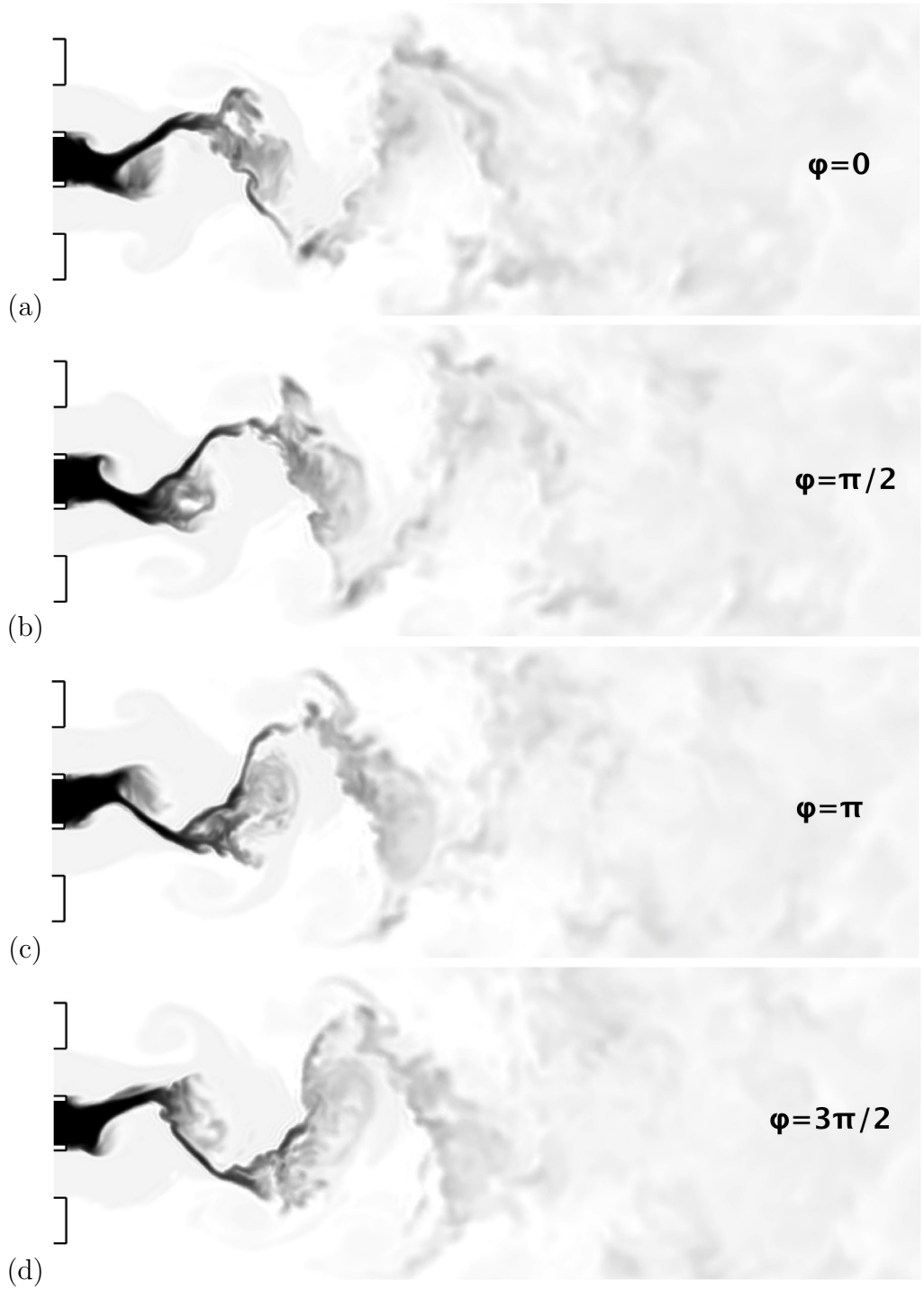

Figure 28: *Case LarThin*^{2}. Longitudinal slices of instantaneous density during 4 phases ϕ of one period (a) $\phi = 0$ (b) $\phi = \pi/2$ (c) $\phi = \pi$ (d) $\phi = 3\pi/2$.

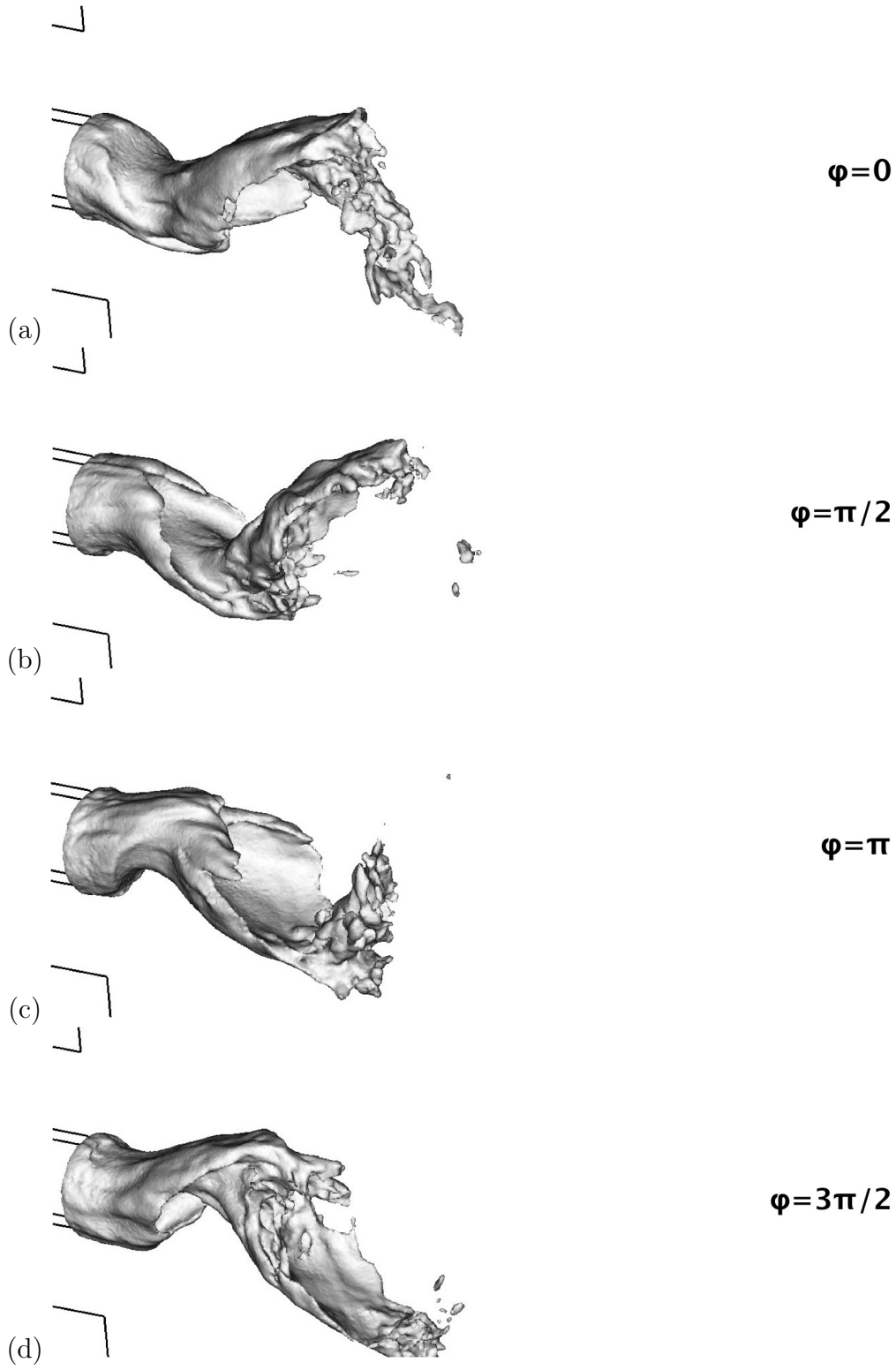

Figure 29: *Case LarThin*[2]. Phase averaged density iso-surfaces (86 kg m^{-3}) during 4 phases ϕ of one period (a) $\phi = 0$ (b) $\phi = \pi/2$ (c) $\phi = \pi$ (d) $\phi = 3\pi/2$.

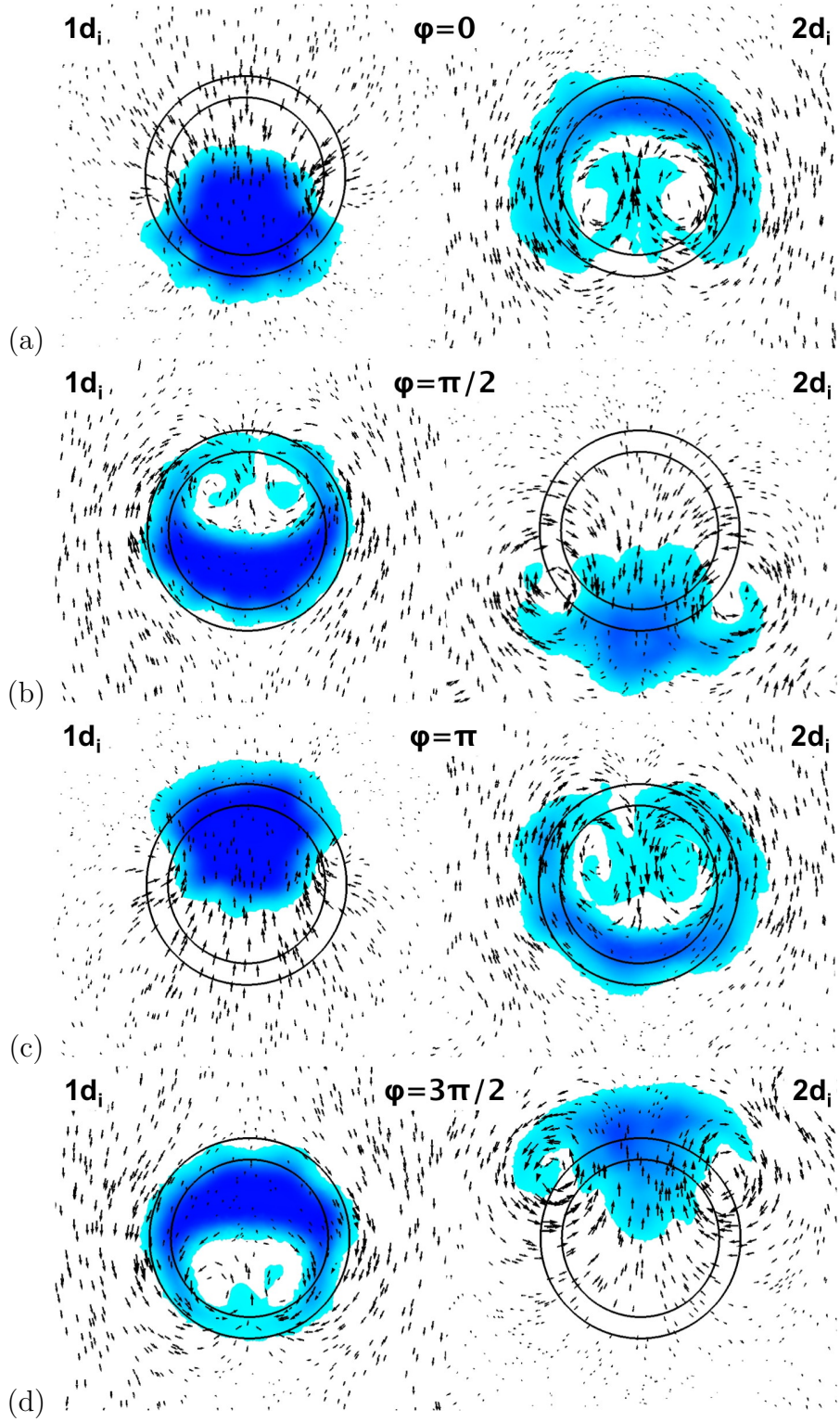

Figure 30: *Case LarThin*[2]. Phase averaged transverse slices of density (blue) with velocity vectors during 4 phases ϕ of one period (a) $\phi = 0$ (b) $\phi = \pi/2$ (c) $\phi = \pi$ (d) $\phi = 3\pi/2$. The slices are positioned at $x = d_i$ and $x = 2d_i$ from the injector exit.

6.4.2 Case SarThick

As outlined previously in Sec. 6.3.2, this case is less influenced by the acoustic modulation than case LarThin. Examining the iso-surfaces of density shown in Fig. 31 one observes a transverse motion of the outer mixing layer close to the outer injection channel. This motion is hardly visible in the instantaneous images but can be revealed by phase averaging. The coherent motion induced by the acoustic modulation is highlighted in Fig. 32. Due to the lip thickness, the central core itself is hardly perturbed by the modulation. On its periphery, an alternate release of vortices is generated by the transverse acoustic waves.
This is confirmed in Fig. 33 where two cuts of density at $d_i/2$ and d_i are presented for four different phases in an acoustic cycle. The velocity field induced by the transverse modulation is shown to promote the alternate release of vortices.

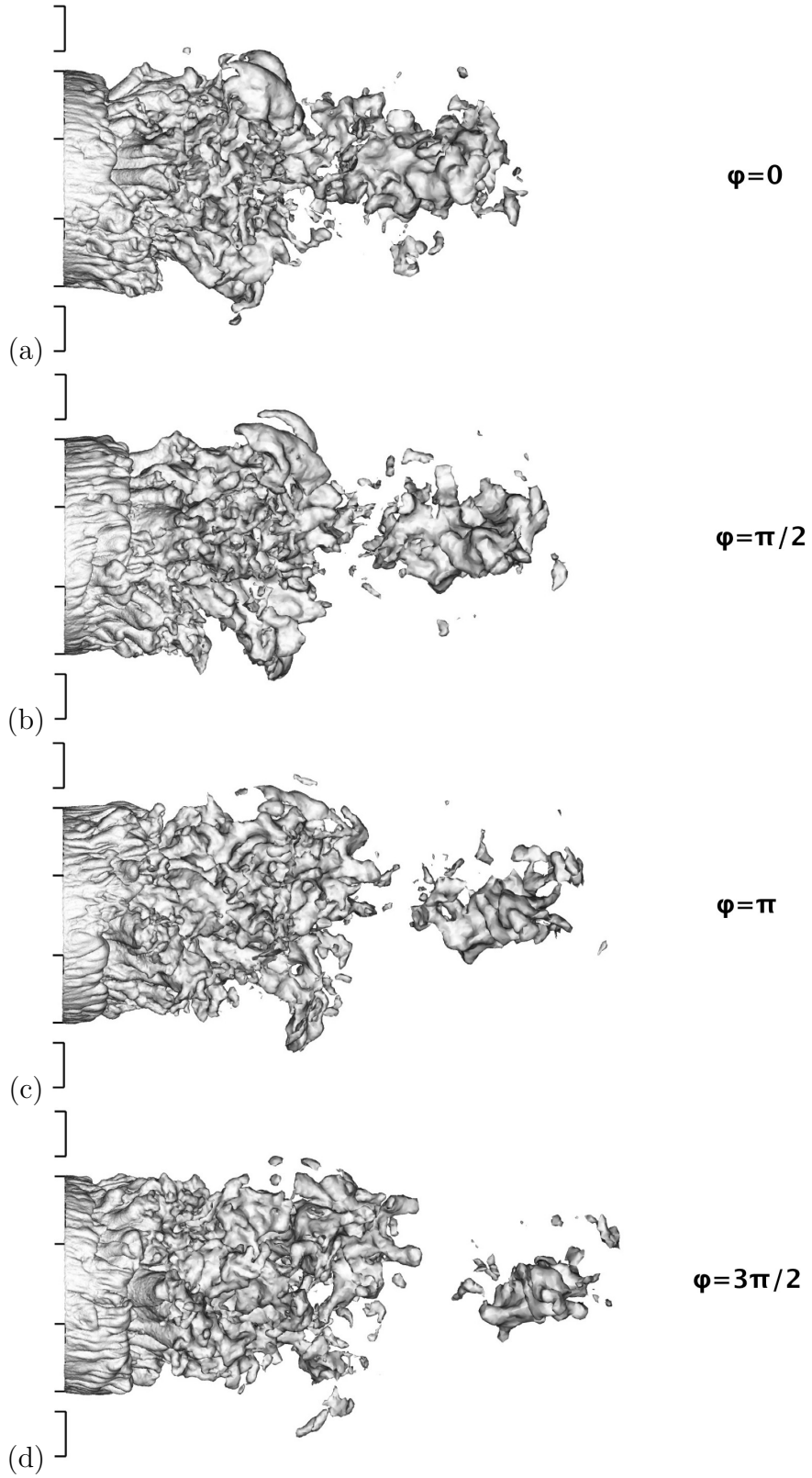

Figure 31: *Case SarThick*^{2}. Density iso-surface (100 kg m^{-3}) during 4 phases ϕ of one period (a) $\phi = 0$ (b) $\phi = \pi/2$ (c) $\phi = \pi$ (d) $\phi = 3\pi/2$.

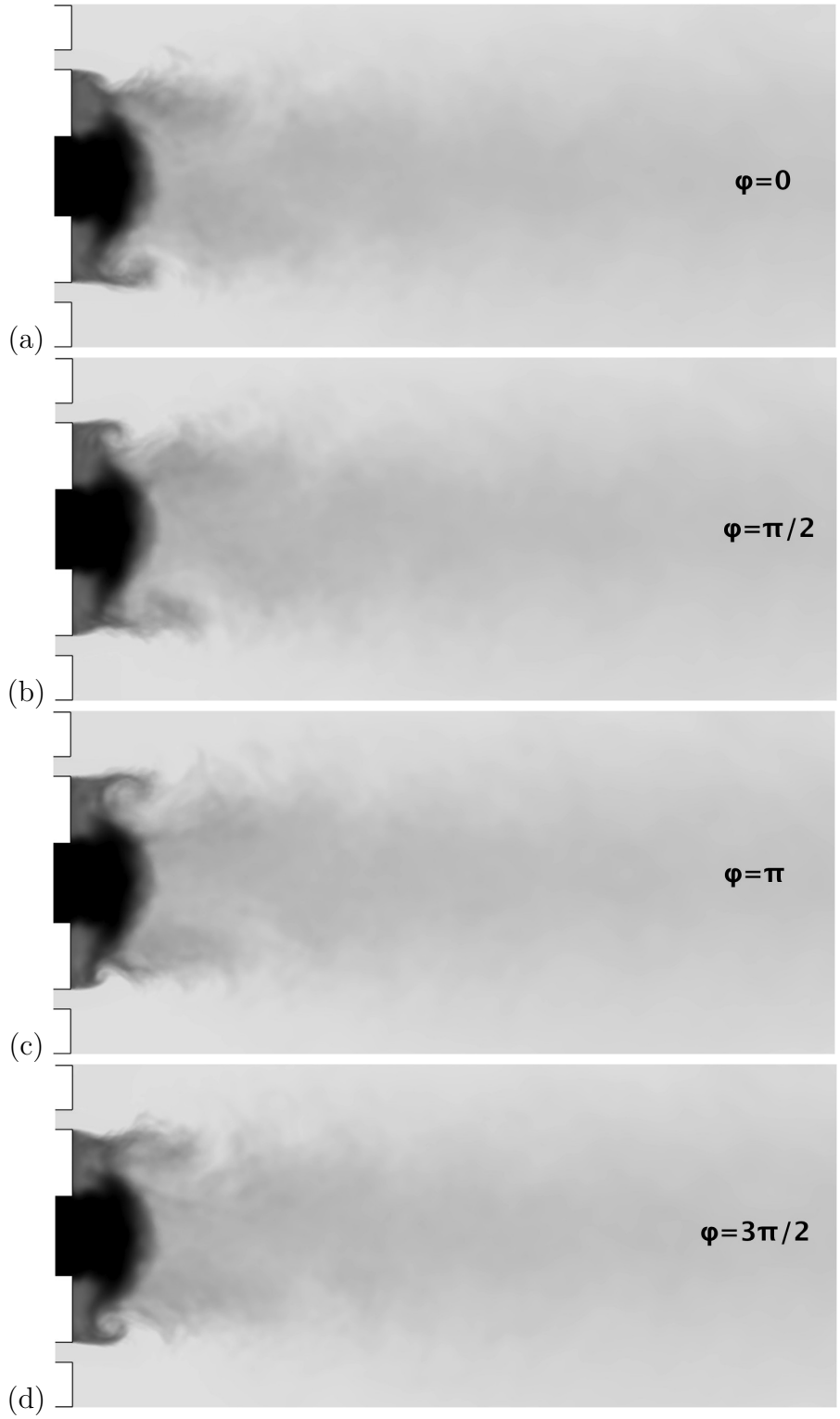

Figure 32: *Case SarThick*^{2}. Phase averaged longitudinal slices of density during 4 phases ϕ of one period (a) $\phi = 0$ (b) $\phi = \pi/2$ (c) $\phi = \pi$ (d) $\phi = 3\pi/2$.

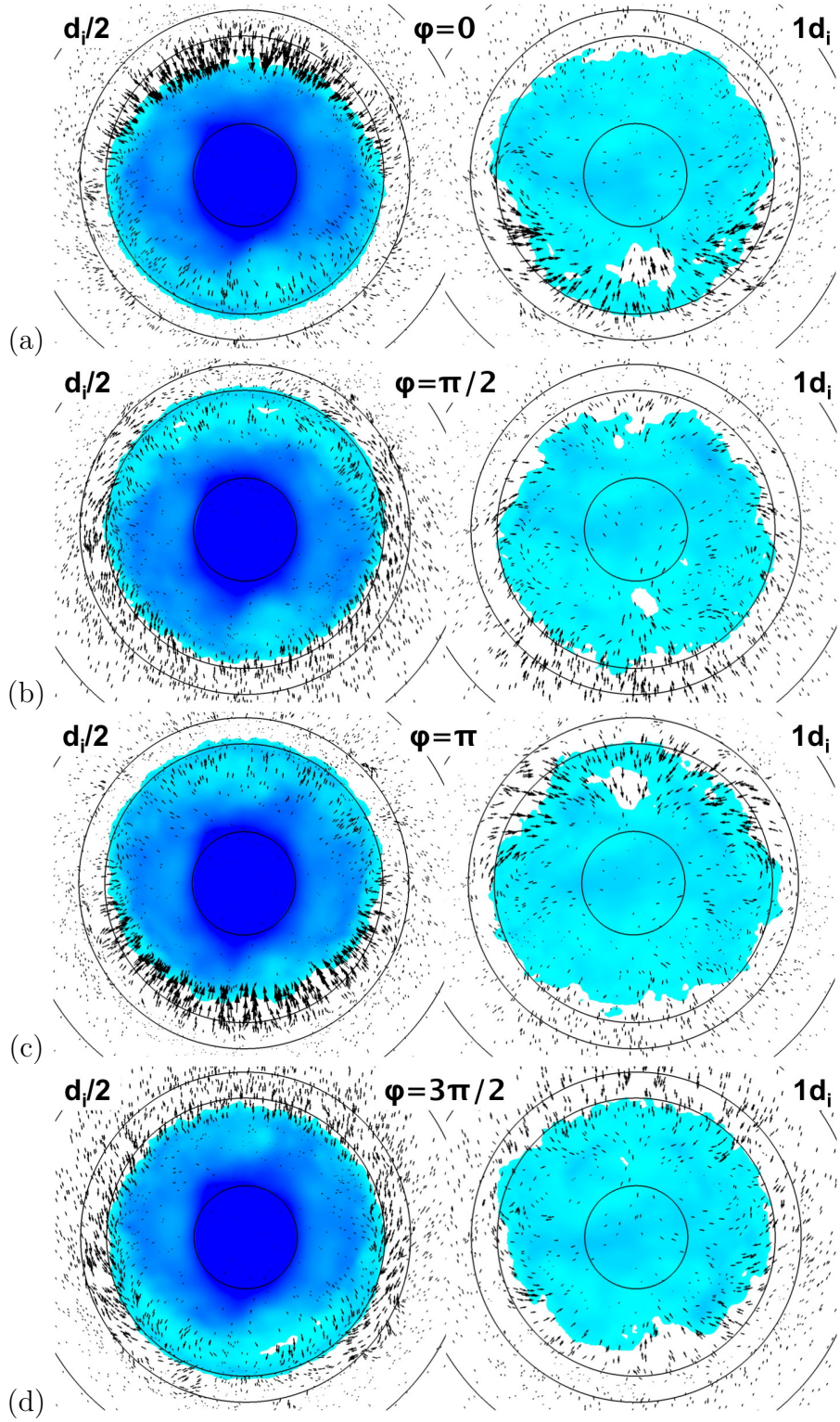

Figure 33: *Case SarThick*^{2}. Phase averaged transverse slices of density (blue) with velocity vectors during 4 phases ϕ of one period (a) $\phi = 0$ (b) $\phi = \pi/2$ (c) $\phi = \pi$ (d) $\phi = 3\pi/2$. The slices are positioned at $x = 0.5d_i$ and $x = d_i$ from the injector exit.

7 Conclusions

Results of Large Eddy Simulations of two experimental configurations from AFRL, Edwards, are reported in this document. These two injection systems operate at high pressure above the critical value requiring real gas representations of the equation of state and thermodynamics. The two experimental conditions feature large differences in terms of flow dynamics and response to an acoustic modulation. In the case of a large aspect ratio injector featuring a thin lip separating the coaxial streams (LarThin), the flow is close to a classical coaxial jet geometry. In the second case (SarThick) characterized by a small aspect ratio and a thick lip between the two injected streams. a large back flow region is established around the inner jet. This region strongly confines the inner jet and enhances mixing. Simulations are compared with experimental data in the absence or in the presence of acoustic modulation. It is shown that the jet geometry is suitably retrieved both in absence of modulation or under transverse acoustic forcing. Simulations under acoustic modulation capture the main coupling phenomena. Under acoustic modulation, the case LarThin features a large scale flag-like motion with an important jet length reduction. The acoustic modulation produces large scale counter-rotating vortices which stretch the inner jet and enhance the mixing process. In the case SarThick, the acoustic modulation has a limited effect on the coaxial jet geometry, probably because of the presence of the dynamical back flow that dominates mixing in the injector near field. It is found however that modulation has an important effect on the jet penetration length. It is suggested that large eddy simulations can be used to guide injector selection which could lead to a lesser sensitivity to external modulation which could be beneficial to a stable operation of the propulsion system.

Acknowledgment

The authors wish to thank Dr. Ivett Leyva for suggesting this investigation and providing the experimental data and for many helpful discussions. The AVBP solver used for this study has been developed at Cerfacs. This work was granted access to the HPC resources of CINES under the allocation 2013 - 2b6176 made by GENCI (Grand Equipement National de Calcul Intensif). This work has been carried out under award FA8655-12-1-2047 from EOARD monitored by LtCol Brad Thompson and LtCol Kevin Bollino.

References

[1] J. Bellan. Supercritical (and subcritical) fluid behavior and modeling: drops, streams, shear and mixing layers, jets and sprays. *Progress in Energy and Combustion Science*, 26:329–366, 2000.

[2] T.H. Chung, M. Ajlan, L.L. Lee, and K.E. Starling. Generalized multiparameter correlation for nonpolar and polar fluid transport properties. *Industrial & Engineering Chemistry Research*, 27(4):671–679, 1988.

[3] O. Colin and M. Rudgyard. Development of high-order taylor-galerkin schemes for unsteady calculations. *Journal of Computational Physics*, 162(2):338–371, 2000.

[4] I. A. Leyva, J. Rodriguez, B. Chehroudi, and D. Talley. Preliminary results on coaxial jet spread angles and the effects of variable phase transverse acoustic fields. In *46th AIAA Aerospace Sciences Meeting and Exhibit, Reno, Nevada, Jan. 7-10*, volume AIAA-2008-950, 2008.

[5] R. S. Miller, K. G. Harstad, and J. Bellan. Direct numerical simulation of supercritical fluid mixing layers applied to heptane-nitrogen. *Journal of Fluid Mechanics*, 436:1–39, 2001.

[6] V. Moureau, G. Lartigue, Y. Sommerer, C. Angelberger, O. Colin, and T. Poinsot. High-order methods for DNS and LES of compressible multi-component reacting flows on fixed and moving grids. *Journal of Computational Physics*, 202(2):710–736, 2005.

[7] F. Nicoud and F. Ducros. Subgrid-scale stress modelling based on the square of the velocity gradient. *Flow, Turbulence and Combustion*, 62(3):183–200, 1999.

[8] J.C. Oefelein. Mixing and combustion of cryogenic oxygen-hydrogen shear-coaxial jet flames at supercritical pressure. *Combustion Science and Technology*, 178(1):229–252, 2006.

[9] N. Okong'o and J. Bellan. Consistent boundary conditions for multicompoment real gas mixtures based on characteristic waves. *Journal of Computational Physics*, 176:330–344, 2002.

[10] D. Peng and D. B. Robinson. A new two-constant equation of state. *Ind. Eng. Chem. Fundam.*, 15:59–64, 1976.

[11] T. Poinsot and S. Lele. Boundary conditions for direct simulations of compressible viscous flows. *Journal of Computational Physics*, 101(1):104–129, 1992.

[12] B. E. Poling, J. M. Prausnitz, and J. P. O'Connel. *The properties of gases and liquids*. McGraw-Hill, fifth edition, 2001.

[13] C. Rey, S. Ducruix, and S. Candel. A method for the transverse modulation of reactive flows with application to combustion instability. *Combustion Theory and Modelling*, 9:5–22, 2005.

[14] J. Rodriguez, J. Graham, I. Leyva, and D. Talley. Effect of Variable Phase Transverse Acoustic Fields on Coaxial Jet Forced Spread Angles. In *47th AIAA Aerospace Sciences Meeting*, volume AIAA-2009-231. American Institute of Aeronautics and Astronautics, 2009.

[15] J. Rodriguez, I. Leyva, J. Graham, and D. Talley. Mixing Enhancement of Liquid Rocket Engine Injector Flow. In *45th AIAA/ASME/SAE/ASEE Joint Propulsion Conference and Exhibit, Denver, Colorado, Aug. 2-5*, volume AIAA-2009-5143, 2009.

[16] T Schmitt, J Rodriguez, IA Leyva, and S Candel. Experiments and numerical simulation of mixing under supercritical conditions. *Physics of Fluids*, 24(055104):29, 2012.

[17] T. Schmitt, L. Selle, A. Ruiz, and B. Cuenot. Large-Eddy Simulation of Supercritical-Pressure Round Jets. *AIAA journal*, 48(9):2133–2144, 2010.

[18] Thomas Schmitt, Yoann Méry, Matthieu Boileau, and Sebastien Candel. Large-eddy simulation of oxygen/methane flames under transcritical conditions. *Proceedings of the Combustion Institute*, 33(1):1383–1390, 2011.

[19] T. Schönfeld and T. Poinsot. Influence of boundary conditions in LES of premixed combustion instabilities. In *Annual Research Briefs*, pages 73–84. Center for Turbulence Research, NASA Ames/Stanford Univ., 1999.

[20] A. Smirnov, S. Shi, and I. Celik. Random flow generation technique for large eddy simulations and particle-dynamics modeling. *Trans. ASME. Journal of Fluids Engineering*, 123:359–371, 2001.

[21] V. Yang. Modeling of supercritical vaporization, mixing, and combustion processes in liquid-fueled propulsion systems. *Proceedings of the Combustion Institute*, 28(1):925–942, 2000.

Nomenclature

Injector and mesh characteristics

δ_l	inner lip thickness
S_e	outer injector section surface
S_i	inner injector section surface
d_i	inner injector diameter
h_e	outer injector diameter
Δ_t	time step
τ_c	convective time
$\Delta_{x,min}$	minimum characteristic cell size

Injection conditions

T_i	inner injector injection temperature
T_e	outer injector injection temperature
u_i	inner injector injection bulk velocity
u_e	outer injector injection bulk velocity
ρ_i	inner injector injection density
ρ_e	outer injector injection density
$J = (\rho_e u_e^2)/(\rho_i u_i^2)$	momentum flux ratio
$M = (\rho_e u_e)/(\rho_i u_i)$	mass flux ratio
$S = \rho_e/\rho_i$	density ratio
$U = u_e/u_i$	velocity ratio

Governing equations and thermodynamics

$\boldsymbol{w}$	conservative variables vector
ρ	Density
$\boldsymbol{u}$	velocity vector
E	total energy
e_s	internal energy
e_k	kinetic vector
p	pressure
$\boldsymbol{x}$	spatial coordinate vector
x	axial distance from injector
t	time
$\boldsymbol{\tau}$	viscous stress tensor
$\boldsymbol{q}$	heat flux vector
$\boldsymbol{\tau^t}$	subgrid scale stress tensor
$\boldsymbol{q^t}$	subgrid scale heat flux vector
λ	subgrid scale conductivity
C_p	heat capacity at constant pressure
Pr_t	turbulent Prandlt number
μ_t	turbulent dynamic viscosity
T	temperature
R	perfect gas constant
W	molar mass
T_c	critical temperature
p_c	critical pressure
ω	acentric factor
T_R	reduced temperature

Acoustic

f	acoustic modulation frequency
u'_{ac}	peak to peak acoustic velocity modulation amplitude
ϕ	phase in a modulation period

Jet length scales

L_ρ^{ic}	intact core length
$L_\rho^{ic,0}$	intact core length of the unmodulated case